

Effect of wind speed gradients on AEP in a wind farm cluster

Department of
Wind Energy
Master Report

Patrick Arthur Redmond Duffy

DTU Wind Energy-M-0320

August 2019

DTU Wind Energy
Department of Wind Energy



Author: Patrick Arthur Redmond Duffy

Title: Effect of wind speed gradients on AEP in a wind farm cluster

DTU Wind Energy-M-0320

August 2019

Project period:

November 2018 – August 2019

ECTS: 45

Education: Master of Science

Supervisor:

Alfredo Peña

Paul van der Laan

DTU Wind Energy

Simon Watson

TU Delft

Nicolai Gayle Nygaard

Ørsted

Remarks:

This report is submitted as partial fulfillment of the requirements for graduation in the above education at the Technical University of Denmark.

DTU Wind Energy is a department of the Technical University of Denmark with a unique integration of research, education, innovation and public/private sector consulting in the field of wind energy. Our activities develop new opportunities and technology for the global and Danish exploitation of wind energy. Research focuses on key technical-scientific fields, which are central for the development, innovation and use of wind energy and provides the basis for advanced education at the education.

We have more than 240 staff members of which approximately 60 are PhD students. Research is conducted within nine research programmes organized into three main topics: Wind energy systems, Wind turbine technology and Basics for wind energy.

Technical University of Denmark

Department of Wind Energy

Frederiksborgvej 399

2800 Kgs. Lyngby

Denmark

www.vindenergi.dtu.dk

Acknowledgments

I am lucky to have studied in a program like the European Wind Energy Master, and I owe many people for their help on my journey.

I would like to first thank my thesis supervisors from DTU Wind Energy and TU Delft - Paul van der Laan, Alfredo Peña, and Simon Watson. Their questions and feedback during our discussions encouraged me to think deeply about the decisions I made during my thesis work and helped me to continue developing my analytical thinking as an engineer. I am especially thankful for Paul's responsiveness to questions and assistance with surprises.

I also appreciate the love and support that my family, girlfriend, and friends offered to me as I took on the challenges of an international joint master program and throughout my thesis work. Their encouragement helped me to stay grounded when I struggled, and their phone calls brightened my days.

Finally I am incredibly grateful for the opportunity to study in an international environment filled with inspiring people. I love being a part of the EWEM and DTU communities, and I know I will carry many of these friendships with me for the rest of my life.

Abstract

The engineering flow models used to estimate annual energy production (AEP) in offshore wind farm layout optimization typically assume inflow homogeneity over the model domain. This assumption lies in contrast with observations of horizontal wind speed gradients in coastal regions where many offshore wind farms are being constructed. Accounting for wind speed gradients in wind farm models may lead to reduced uncertainty in AEP estimates and reduced bias in optimized wind farm layouts. This thesis examines whether accounting for horizontal wind speed gradients with WRF simulated wind resource inputs to engineering wake models impacts AEP prediction for a wind farm cluster in the Irish Sea by comparing results with calculation methods which assume homogeneous inflow.

Analysis of a wake free two turbine case under a gradient shows that the assumption of homogeneity leads to errors with the true power which a gradient based method is able to predict. Despite this, results suggest that the overall impact of modelling wind speed gradients on AEP predictions in the Irish Sea cluster is small. Homogeneous and gradient methods using the same wind resource data predicted differences in AEP of between 0.1% and 0.75%, with most cases below 0.75%. Filtering by wind direction reveals AEP differences larger than the assumed wake model uncertainty for two sectors with inflow from land. The AEP contribution from sectors with mean wind speed gradients is limited by low frequencies and mean wind speeds. Additionally, positive and negative power differences predicted by homogeneous and gradient methods were found to balance over the year.

Contents

1	Introduction	1
2	Background	3
2.1	Annual energy production (AEP)	3
2.2	Wind turbine wakes	3
2.3	Wakes and wind farms	4
2.4	Wake modeling	5
2.5	Uncertainty in AEP	6
2.6	Coastal flows	7
3	Test site specifications	9
4	Methods	12
4.1	Definitions	12
4.2	WRF wind climate at the test site	12
4.3	Wind farm flow models	14
4.3.1	Jensen wake model	15
4.3.2	Gaussian wake model	17
4.3.3	Choice of model coefficients	19
4.3.4	Wake superposition methods	19
4.4	PyWake	19
4.5	AEP calculation methods	21
4.5.1	Time series based methods	21
4.5.2	WAsP grid based methods	27
4.6	Wake free reference power	29
4.6.1	Time series based wake-free reference power	29
4.6.2	WAsP grid based wake-free reference power	30
4.7	Model uncertainty	30
5	Results	31
5.1	A simplified case	31
5.1.1	Flow direction 1: wake free conditions ($\theta = 0^\circ$)	32
5.1.2	Flow direction 2: WT 2 waked ($\theta = 270^\circ$)	34
5.2	Barrow AEP	36
5.2.1	Time series based calculations	36

5.2.2	WAsP grid based calculations	40
5.2.3	Time series based sector-wise Barrow AEP	42
5.2.4	Barrow wind farm efficiency	43
5.3	Cluster AEP	45
5.3.1	Time series based calculations	46
5.3.2	WAsP grid based calculations	47
5.3.3	Time series based sector-wise cluster AEP	48
5.4	Uncertainty	48
6	Conclusions and Future Work	50
	Appendices	52
A	Wind farm maps	53
B	WRF wind climate maps - Additional heights	54
	Bibliography	58

List of Symbols

A	Area
$ AEP$	Annual energy production
C_T	Thrust coefficient
D	Rotor diameter
D_w	Wake diameter at downstream distance x
N	Some Number
N_{ref}	Some reference number
P	Power
P_{act}	Actual power production
$P_{i,j}$	Power of turbine i and time step j
P_{ref}	Reference power production
$P_{tot,j}$	Total wind farm or wind farm cluster power at time step j
T	Thrust force
TI	Turbulence intensity
U	Wind speed
U_r	Wind velocity just behind rotor
$V(x)$	Velocity at downstream distance x
$V_{x,m}$	Stream-wise component of the m^{th} unit vector in a set
$V_{y,m}$	Crosswind component of the m^{th} unit vector in a set
$\% \Delta$	Percent change compared to some reference
ΔU	Velocity deficit in the wake
Δx	Distance between two points
Θ	A constant angle in [deg]

η_{wf}	Wind farm efficiency
\bar{U}_j	Average wind speed
$\bar{\theta}$	Vector averaged wind direction in [deg]
ϕ_m	Wind direction m in a set [rad]
ρ	Density
σ	Standard deviation of Gaussian-like velocity deficit profile
θ_{ij}	Wind direction [deg] at turbine i and time step j
a	Axial induction factor
e_{ij}	Effective wind speed at turbine i and time step j
i	Turbine i
j	Time step j
k	Wake expansion parameter, Weibull shape parameter, or a wind direction in a set when noted as such
$p(x)$	Probability
r	Radial distance from rotor/ wake center
u_m	Stream-wise component of wind velocity m in a set
u_{wm}	Wake model uncertainty estimate as a percentage of AEP
v_m	Crosswind component of wind velocity m in a set
x	Distance downstream
$C(x)$	Max normalized wake center velocity deficit at downstream distance x

List of Figures

- 3.1 Maps of the site (a) in the Irish Sea with cluster in red and (b) the wind farms in the cluster (geospatial data from Hijmans (2019)) 9
- 3.2 Barrow offshore wind farm 10
- 3.3 Power P and thrust coefficient C_T curves for the turbines in the modeled wind farms 11

- 4.1 WRF simulated wind roses at turbine hub heights for (a) BOW-B05 and (b) WOW01-F01 for the year starting 00:00:00 on October 1st, 2014 14
- 4.2 Normalized mean WRF wind speeds per wind direction sector at 75 [m]. Bounds of the map area are [456583, 482818] and [5976479, 5998679] in [m] for UTM zone 30 Easting and Northing, respectively. Normalization wind speed presented in the subfigure captions. 15
- 4.3 Control volume just behind turbine from Katić, Højstrup, and N. O. Jensen (1987) for derivation of Jensen wake model. Rotor plane indicated in with a solid blue line 16
- 4.4 Control volume around turbine (Fig. 2b from Bastankhah and Porté-Agel (2014)) for derivation of Gaussian wake model. Rotor plane indicated in with a solid blue line 18
- 4.5 PyWake AEP calculation flowchart from PyWake documentation (DTU 2019) . . 20
- 4.6 Flowchart depicting naming procedure for the five methods used in the AEP calculation 22
- 4.7 Graphic depicting a simple two turbine wind farm for illustrating the methods . . 25
- 4.8 Illustration of four turbine verification case with $\Delta x = \Delta y = 1000$ [m] 26
- 4.9 Comparison of G.all and H.all calculation approaches for a test case. Values matched the reference. 27
- 4.10 Illustration highlighting need for interpolation between wind resource grid levels . 29

- 5.1 Wind speeds for range of $\frac{2\Delta U}{U_{rated}}$ 32
- 5.2 P_1 vs. $\frac{2\Delta U}{U_{rated}}$ 32
- 5.3 Total wind farm power, P_{tot} predicted by the different methods 33
- 5.4 $\% \Delta$ in total wind farm power w.r.t true for the different methods 33
- 5.5 Turbine powers (a) P_1 and (b) P_2 predicted by the different methods for $\Delta x = 7D$ 35
- 5.6 Effect of gradients and turbine spacing in the waked situation 35
- 5.7 Percent change in AEP relative to the reference value for cases where (a) only Barrow is modeled and (b) the whole cluster is modeled with the time series based calculation methods 37

5.8	75 [m] normalized mean wind speeds for Sector 4 across (a) Barrow and (b) zoomed out to the wind farm cluster. Values are normalized by the mean speed at turbine BOW - B05, shown in purple	38
5.9	Time series based (a) Barrow wind farm efficiency η_{BOW} and (b) percent change between wake-free AEP values and the reference case AEP (time series based, NOJ, $k=0.04$, Barrow WT modeled)	39
5.10	Percent change in WAsP grid Barrow AEP relative to reference case (time series based H.point, NOJ, $k=0.04$, 30 WT modeled) for (a) 30 WT and (b) 270 WT cases	40
5.11	WAsP grid based (a) Barrow wind farm efficiency η_{BOW} and (b) percent change between wake-free AEP values and the reference case AEP (time series based, NOJ, $k=0.04$, Barrow WT modeled)	41
5.12	Sector-wise percent change in Barrow AEP relative to reference case. Only turbines from Barrow are modeled (30 WT)	43
5.13	Sector-wise percent change in Barrow AEP relative to reference case. Turbines from the entire cluster are modeled (270 WT)	44
5.14	Sector-wise Barrow AEP results in [GWh] from time series based H.point methods with $k=0.04$, linear wake summation. 30 WT indicates only Barrow was modeled and 270 WT indicates that the turbines from the entire cluster are included. Wind direction sector bin count based on the filtering wind direction at BOW-B05 indicated in red	45
5.15	Barrow wind farm efficiency by direction - in stages	45
5.16	Time series based (a) percent change between AEP values and the reference case AEP and (b) cluster efficiency $\eta_{cluster}$	46
5.17	Year long time series of power difference predicted by the H.all and G.all time series methods. Day 1 corresponds to 1 October, 2014	47
5.18	WAsP grid based cluster (a) AEP results and (b) cluster efficiency	47
5.19	Sector-wise cluster AEP results for different methods presented as percent change relative to the reference case (time series based H.point with $k=0.04$). Filtered based on the wind direction time series at BOW-B05	48
A.1	Wind farm maps	53
B.1	Normalized WRF \bar{U} per sector at 83.5 [m]	55
B.2	Normalized WRF \bar{U} per sector at 90 [m]	56
B.3	Normalized WRF \bar{U} per sector at 100 [m]	57

List of Tables

- 3.1 Key parameters of the wind farm cluster 10
- 4.1 Hypothetical wind conditions for the verification case 27
- 5.1 Barrow H.point AEP [MWh] estimates with and without wake effects, modeling turbines from Barrow only and from the entire cluster 39
- 5.2 Barrow H.point WAsP grid based AEP [MWh] results with and without wake effects, modeling Barrow only and the wind farm cluster 41
- 5.3 Barrow G.all WAsP grid based AEP [MWh] results with and without wake effects, modeling Barrow only and the wind farm cluster 41
- B.1 \bar{U} [m/s] at turbine BOW-A07 for different direction sectors and heights 54

Chapter 1

Introduction

With the rapid development of offshore wind energy, competition to minimize the cost of energy has led to the clustering of offshore wind farms in coastal regions. Bloomberg New Energy Finance projects in BNEF (2017) that global cumulative offshore wind capacity will reach 115 [GW] by 2030, driven by an increasing global customer base. Accurately modelling performance and predicting annual energy production (AEP) of wind farms near the coast has worldwide implications for the financial success of wind energy projects and the growth of a low carbon energy source.

Past modeling efforts have focused on understanding the impact of wind turbine wake losses on energy yield in offshore wind farms, which can be as high as 10-20% of energy production according to R. J. Barthelmie, K. Hansen, et al. (2009). These wake models range in domain size, computational efficiency, and model fidelity as described by Göçmen et al. (2016). The lower fidelity models, known as engineering wake models, serve as industry workhorses in wind farm design and optimization due to their low computational cost. Engineering wake models typically assume homogeneous inflow in the model domain, but this lies in contrast to the observations of R.J. Barthelmie et al. (2007). They found that offshore wind speeds in coastal areas tend to increase with distance from the coast (fetch), leading to horizontal gradients of as much as 2 [m/s] within a wind farm. This matters because ignoring coastal wind speed gradients may bias the results when engineering wake models are used in optimization of the wind farm layout.

More recently, Nygaard (2014) investigated the impacts of turbine wakes from one wind farm on another at a site off the coast of Lolland, Denmark. For overland wind directions the authors noted horizontal wind speed differences larger in magnitude than the wind speed variation due to wake effects. The work of Nygaard and S. D. Hansen (2016) suggests that future uncertainty reductions in energy yield calculations may come from better addressing horizontal wind speed gradients in flow models.

Alfredo Peña, K. S. Hansen, et al. (2017) used the Weather Research and Forecasting (WRF) model to define a wind resource input to engineering wake models in order to account for coastal gradients at Anholt offshore wind farm. The authors found that modeling the wind speed gradients in this way resulted in a predicted AEP for Anholt less than 1% different compared with calculations assuming horizontally homogeneous wind fields. They attribute the small difference to positive and negative errors which cancel over the course of the year, and indicate results to be wind farm specific. Poulsen (2019) utilized the Explicit Wake Parametrisation (EWP) in WRF

simulations and SCADA data to investigate inter wind farm wake effects in a cluster of wind farms in the Irish Sea. These simulations provide an opportunity to further study the impact of wind speed gradients on AEP in a wind farm cluster in a different location.

The objective of this thesis is to examine whether accounting for horizontal wind speed gradients with WRF generated wind resource inputs to engineering wake models impacts AEP prediction in an Irish Sea wind farm cluster by comparing results with calculation methods which assume homogeneous inflow.

The structure of the thesis is as follows. This document first presents background on relevant topics before giving details of the site in the Irish Sea used for the investigation. Next, the methods for analysis are explained. Then, the results are presented and discussed before the essential components of the work are summarized in the conclusion.

Chapter 2

Background

This chapter first discusses the concept of annual energy production (AEP) before providing a few core concepts relating to understanding methods for estimating for AEP of offshore wind farms near the coast.

2.1 Annual energy production (AEP)

The annual energy production is typically calculated as the total energy produced at each wind speed over the course of the year. In discrete form AEP is often computed as the average power produced between two wind speeds multiplied by the probability of wind speeds in that range and multiplied by time, such as in Equation 2.1.

$$AEP = 8760 \sum_{i=1}^{N-1} \frac{1}{2} (P(U_{i+1}) + P(U_i)) p(U_i < U_0 < U_{i+1}) \quad (2.1)$$

Where f is the probability of a wind speed U_0 falling between U_i and U_{i+1} , and P is the power produced at wind speed U_0 . N is the number of wind speed bins, and 8760 is the number of hours in a non-leap year. When multiple turbines are clustered together in a wind farm or even a cluster of wind farms, wind turbine wakes need to be accounted for in the modeling process.

AEP may be thought of as the combined effects of the wind turbines, wind resource, wind farm layout, and wakes.

2.2 Wind turbine wakes

A wind turbine wake forms behind the rotor as the turbine slows the wind and extracts momentum from the flow. In the wake, the flow is characterized by increased turbulence and a velocity deficit compared with the free stream wind, both of which relate strongly to the turbine thrust coefficient. These properties are connected to the main challenges wakes pose to the wind industry. The velocity deficit means less available power and the higher turbulence level means increased loads for downstream wind turbines in the wake.

Two main regions are often identified within the wake- the near wake and the far wake- due to differences in the main flow characteristics. Burton et al. (2009) suggests the near wake is considered to be the region where the influence of the rotor dominates, approximately 1-3 turbine

diameters downstream. In the near wake a cylindrical shear layer separates slower moving fluid in the wake from the free stream. As detailed by Vermeer, J. N. Sørensen, and Crespo (2003), the tip vortices are present in this turbulent shear layer, the thickness of which increases downstream due to turbulent diffusion as the wake expands. R. J. Barthelmie, K. S. Hansen, and Pryor (2013) highlights that the main parameters governing wake expansion include turbulence intensity, wind speed, direction, and atmospheric stability.

Some authors identify a transition region after the shear layer reaches the wake center and before the fully developed far wake region, where turbulence dominates such as Vermeer, J. N. Sørensen, and Crespo (2003). The velocity profile in the far wake has a Gaussian shape according to R. J. Barthelmie, K. S. Hansen, and Pryor (2013). The work of Manwell, McGowan, and Rogers (2009) underscores how turbulent mixing with the free stream (and flow above the wind farm) re-energizes the flow, and this process continues far downstream until no velocity deficit is distinguishable, but turbulence levels remain higher than the free stream. This wake recovery depends on mixing via turbulence intensity and atmospheric stability. Christiansen and C. B. Hasager (2005) were the first to use satellite images to investigate wake recovery. They found, depending on atmospheric conditions, that wakes may persist to downstream distances 5-20 km before recovering to within 2% of free stream wind speed. More recent studies such as Badger et al. (2015), have observed wakes persisting for more than 70 km.

2.3 Wakes and wind farms

Flows through wind farms are complex due to varying atmospheric conditions and interactions between multiple wakes. The magnitude of wake losses depends primarily on wind direction and speed distributions, turbine layout and spacing, turbulence intensity, and atmospheric stability based on the work of R. J. Barthelmie, K. S. Hansen, and Pryor (2013). This is especially true below the rated wind speed where the thrust coefficient is high according to Burton et al. (2009).

Wake losses inside wind farms have been studied by many including R. J. Barthelmie, Frandsen, et al. (2007), R. J. Barthelmie, K. Hansen, et al. (2009), R. J. Barthelmie, Pryor, et al. (2010), R. J. Barthelmie, K. S. Hansen, and Pryor (2013), and wind farm efficiency is often defined as the power produced relative to wake free power production. The work of R. J. Barthelmie, Frandsen, et al. (2007) analyzes measurements of Middelgrunden offshore wind farm in Denmark, which has a single curved row of turbines spaced 2.4 times rotor diameter D , and found average power losses due to wakes to be approximately 10% of total production and a down row TI increase of 20%. R.J. Barthelmie and L. E. Jensen (2010) investigates the impacts of wind distribution, atmospheric stability and wind farm layout at Nysted offshore wind farm. The work of R. J. Barthelmie, Pryor, et al. (2010) compares results of several modeling tools including Wind Application software Program (WAsP), DNV GL's WindFarmer, and a Computational Fluid Dynamic (CFD) approach against measurements at the large Horns Rev offshore wind farm for down row directions corresponding to $7D$, $9.4D$, and $10.4D$. They indicated losses are typically on the order of 10-20% of power production and noted a tendency of engineering wake models to under-predict wake losses in large offshore wind farms, named the 'deep array effect.' In the three cases discussed, authors mentioned the fact that horizontal gradients were not included in engineering models when discussing model weaknesses.

As competition for high wind resource sites has grown, wind farms have been clustered together. A few authors have investigated the impacts of wakes from one wind farm on a downstream wind farm (Nygaard (2014), K. S. Hansen et al. (2015), Nygaard and S. D. Hansen (2016)). Wake effects were observed to affect the downstream wind farm, but primarily for the first few rows. At some positions within the downstream wind farm speedup was observed in the case of Rødsand II and Nysted offshore wind farms. Nygaard (2014) found no evidence of a 'deep array effect' in large offshore wind farms, contrary to the earlier suggestion. At Rødsand II and Nysted offshore wind farms, Nygaard and S. D. Hansen (2016) notes that the wind speed difference due to coastal gradients was more significant than the difference due to wake losses for certain wind direction sectors.

Other authors have analyzed the effects of atmospheric stability (R.J. Barthelmie, Churchfield, et al. 2015), the Coriolis force (van der Laan and N. N. Sørensen 2016), and atmospheric gravity waves (Ollier, Watson, and Montavon 2018) on the flow in offshore wind farms. These highlights the complexity of the physics involved in wake flows and factors influencing variation of wind speed and power over the areas of coastal wind farms.

2.4 Wake modeling

Modeling the flow in the wake of a wind turbine is essential to be able to address the challenges wakes present - energy losses from deficits and greater loads from turbulence. Jens N. Sørensen and Ferreira (2016) show that one of the main challenges associated with analyzing wakes is the different length scales and time scales present. They give the example that length scales could range from 0.001 [m] in the airfoil boundary layer to 100,000 [m] in a wind farm cluster.

This is not a new problem, and despite the fact that computational resources are advancing quickly, the inability to efficiently handle this range of scales has historically forced model developers to make choices about what they want to resolve. Two broad categories include microscale and mesoscale models. A range of models for wakes have been developed with differing fidelity and computational requirements. These include:

- Engineering models (Tophat, Gaussian)
- Reynolds Averaged Navier Stokes (RANS) and Linearized RANS
- Large Eddy Simulation (LES)
- Mesoscale models such as Weather Research and Forecasting (WRF)

The engineering models are usually based on actuator disk theory, empirical observations, or analytical relations. They are typically computationally fast and used for layout optimization. More details regarding engineering models are provided in the Methods section.

RANS models are steady-state CFD models which include the effects of a rotor by directly modeling it or treating it as an actuator disk. The forces in the rotor are computed and all turbulence scales are modeled, often represented by eddy-viscosity models. Laan et al. (2015) used a RANS method with the $k-\varepsilon-f_p$ eddy-viscosity model to simulate flow at three wind farms. Their results, corrected for wind direction uncertainty and compared with measurements, indicated that the $k-\varepsilon-f_p$ model better predicted the power deficit in the near wake than the common $k-\varepsilon$

eddy-viscosity model. The models performed similarly further downstream. Van Der Laan et al. (2015) used a RANS code to simulate the interaction between two neighboring wind farms in the Atmospheric Boundary Layer (ABL). They found that the effect of the Coriolis force has a large influence on the simulation over a large domain (wind farm cluster scale), and recommend including this when studying wind farm wake interaction.

LES models are CFD models which resolve unsteady turbulence down to a certain length and model the small turbulence scales that the chosen numerical grid cannot resolve. The wind turbine forces in LES models are often represented by an actuator line model. These are typically computationally expensive models. Mesoscale models are typically used for weather prediction over large spatial domains on the order of tens to hundreds of kilometers.

Engineering wake models require additional methods to superimpose wakes in situations where there are wakes from multiple turbines which overlap (RANS, LES and WRF do not need this, since the wind turbines interacted in the simulation.). The common techniques for this are linear summation, quadratic summation, and the maximum deficit method Bossuyt (2018). It has been difficult to say with certainty which technique offers the most accurate results, and this is still an area of research. Sometimes model results are computed using more than one summation technique, as was done in Alfredo Peña, K. S. Hansen, et al. (2017).

2.5 Uncertainty in AEP

AEP is an uncertain quantity. Henderson et al. (2014) highlights the fiscal impact of uncertainty in energy production estimates and explores the potential value of uncertainty reductions through different wind measurement technologies. This work underscores that the accuracy of measurement instruments and flow distortion contribute to the overall uncertainty of an energy production estimate based on measurements. Other sources of uncertainty in AEP include inter-annual variability in the wind, spatial variation (highest near the coast), turbine availability, electrical losses, manufacturer power and thrust curves, and wind farm flow models.

The PhD work of Pablo Murcia (2017) underscores the complexity of assessing uncertainty in wind farm flow models, indicating that one of the biggest challenges for wake model validation is the large uncertainties on SCADA derived inflow conditions.

Henderson et al. (2014) notes that it is common to assume a wake model uncertainty of 50% of the loss in energy production estimates. When the uncertainty represents the the standard deviation of a normal distribution, this assumption means that wake models are seen to predict the wake losses to within 50% of the true value about 68% of the time, as Walker et al. (2016) mentions. Walker et al. (2016) benchmarks the performance of four commonly used wake models against production data from five offshore wind farms, finding maximum root-mean-squared errors in validation wake loss below 25%, and suggesting reducing assumed wake model uncertainty to this level.

Nygaard (2015) presents a method for quantifying the uncertainty in wake models based on a bootstrapping method. Nygaard uses this method to compute the relative wake model error for the Jensen wake model based on SCADA data from ten wind farms including Barrow and Walney I. The results indicate that the uncertainty of the Jensen wake model used at the 10 wind farms considered ranged from 1.4% to 5% of the predicted wake loss, with one outlier at 15% of the

predicted wake loss. This work indicated that at some of the wind farms the Jensen wake model slightly underestimated the wake loss, while at others it significantly over-predicted the wake loss.

The authors in R. J. Barthelmie, K. Hansen, et al. (2009) highlight that when comparing many wake model implementations to measurements, the general behavior is often captured qualitatively, but the model predictions frequently deviate from one another, offering a fair degree of uncertainty. This general trend is similar to the results observed by Moriarty et al. (2014), IEA Task 31 (Wakebench), which sought to establish a framework for benchmarking microscale wake models suitable for wind farm development. The findings indicate that increasing model fidelity does not lead to a higher level of accuracy when compared with observations, and that none of the models clearly outperforms the others. The models investigated performed worst in the near wake region, likely due to the fact that most do not directly model the effects of the rotor. Even more sophisticated models, which may better simulate flow behavior, are dependant on the scope and quality of measurements used to define the inflow, which Moriarty et al. (2014) indicates is essential focal point for improving future validations.

One other element which Moriarty et al. (2014) touches on is the fact that wind direction uncertainty and wind direction sector size play a role when comparing turbine observations with wake models. Gaumond, P.-E. ; Réthoré, et al. (2013) explores this with an investigation of wind direction uncertainty in measurements, emphasizing that its relative significance becomes more pronounced when data are binned into small wind direction sectors. They also proposed the application of a Gaussian filter to help correct for this uncertainty when comparing measurements with model predictions.

The Danish Wind Energy Association (DWEA 2003) suggests that uncertainty in manufacturer power curves can be more than 10%, even when certified according to the standards set by the International Electrotechnical Commission (IEC) in standard 61400-12-1. Density variation, wind speed and direction measurements, and turbulence, and wind shear contribute to power curve uncertainty.

2.6 Coastal flows

Frequently, offshore wind farms are constructed near the coastline. Several authors have researched the effects from the transition from land to sea which complicates the flow. Pryor and R. J. Barthelmie (1998) describes the formation of a new boundary layer after this coast to sea transition, and underscores that the wind speed distribution in the coastal zone depends on both fetch and atmospheric stability.

RJ. Barthelmie et al. (2007) highlights how flow in the coastal zone is challenging to model due to the surface roughness discontinuity at the coastline, the influence of onshore topography, and thermal gradients. For three offshore wind farms in Denmark they use mesoscale simulations, remote sensing, and in-situ data to show that vertical wind speed profiles are not in equilibrium with the sea surface over fetches ranging from up to 20 [km] or as high as 70 [km]. They recommend this range to define the coastal zone width in Northern Europe, indicating that this width, and the presence of horizontal wind speed gradients, depend on atmospheric stability. They observed horizontal wind speed gradients as high as 2 [m/s] over a wind farm area.

Wang et al. (2014) compares WRF simulations with data from a Lidar and anemometer measurement campaign in the coastal zone in Lake Erie to better understand the formation of the coastal atmospheric boundary layer (CABL). They noted that for flow moving from land to sea the CABL had not fully developed at a distance of 7 [km] offshore.

van der Laan, A. Peña, et al. (2017) investigates the coastal flow effects on Anholt offshore wind farm using a RANS model, the results of which compared well with mesoscale model simulations and turbine power measurements. The RANS model captured the trends of the horizontal wind speed gradient at the wind farm, despite modelling challenges which are discussed.

Chapter 3

Test site specifications

The test site investigated is a cluster of wind farms located in the northeast portion of the Irish Sea, between the Isle of Man and the British coastal town of Barrow-in-Furness. This chapter presents specifications of the individual wind farms in the cluster.

The cluster of wind farms presently includes the following offshore wind farms (with abbreviations): Barrow (BOW), Walney Phase I (WOW01), Walney Phase II (WOW02), Ormonde (OOWF), West of Duddon Sands (WDS), and the Walney Extension {Walney Phases III and IV (WOW03 and WOW04)}. An area map is presented in Figure 3.1a, with the whole cluster shown in red. The map presented in Figure 3.1b highlights each wind farm in a different color. Walney Phases III and IV are shown in gray since Poulsen (2019)'s WRF simulations cover a period before their construction, and they are not considered in either her work or the present work.

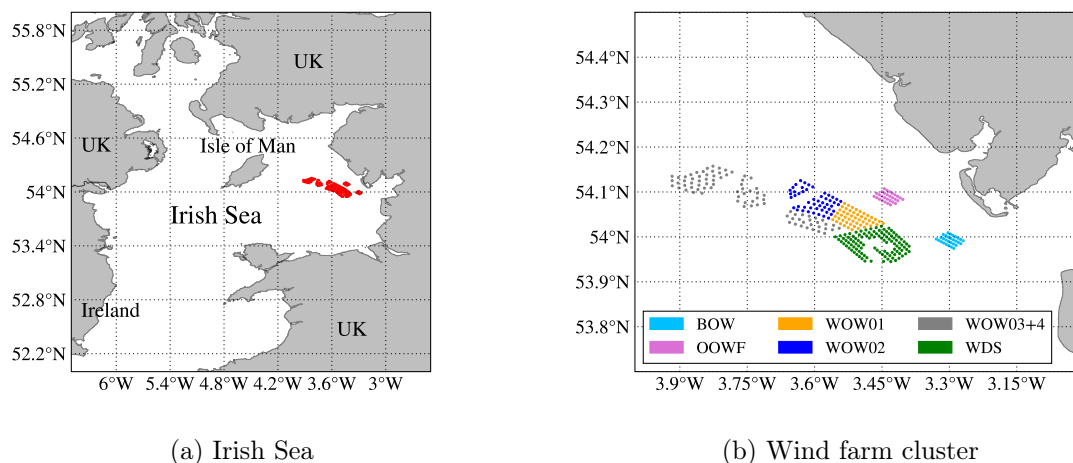


Figure 3.1: Maps of the site (a) in the Irish Sea with cluster in red and (b) the wind farms in the cluster (geospatial data from Hijmans (2019))

The nearest coastline is visible in Figure 3.1b. Note that the shortest fetch from a turbine near the center of Barrow (BOW-B05) is approximately 12.5 [km]. From a turbine near the center of the cluster (WOW01-F01) the shortest fetch is approximately 20 [km], indicating that the wind farm cluster is well within the coastal zone boundary (20-70 [km]) suggested by R.J. Barthelmie et al. (2007).

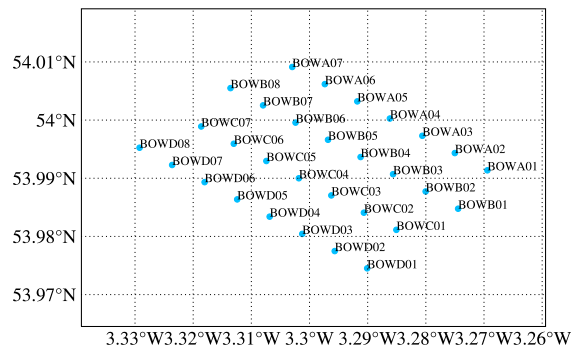


Figure 3.2: Barrow offshore wind farm

A map illustrating the names of the turbines in Barrow is shown in Figure 3.2 since some are referred to specifically. Maps of the wind farms built before 2015 are included in Appendix A.

Key data about each wind farm is presented in Table 3.1, obtained from Poulsen (2019). These data include wind farm capacity, commissioning year, the number and model of the turbines, as well as rotor diameters, and hub heights for all of the turbines in the cluster. The power curves and thrust coefficient curves are used in the analysis are presented in Figure 3.3, also obtained from Poulsen (2019). Both Walney II and West of Duddon Sands use the same turbine model.

Wind Farm	Owner	Cap. MW	Comm. Year	No. Turb.	Turb.	Rotor Diam. m	Hub Height m aMSL
BOW	Ørsted	90	2006	30	V90-3.0MW	90	75
WOW01	Ørsted	183.6	2011	51	SWT-3.6-107	107	83.5
WOW02	Ørsted	183.6	2012	51	SWT-3.6-120	120	90.15
OOWF	Vattenfall	150	2012	30	Senvion 5M	126	90
WDS	Ørsted	389	2014	108	SWT-3.6-120	120	90
WOW03	Ørsted	330	2018	40	V164-8.0MW	164	105
WOW04	Ørsted	329	2018	47	SWT-7.0-154	154	105

Table 3.1: Key parameters of the wind farm cluster

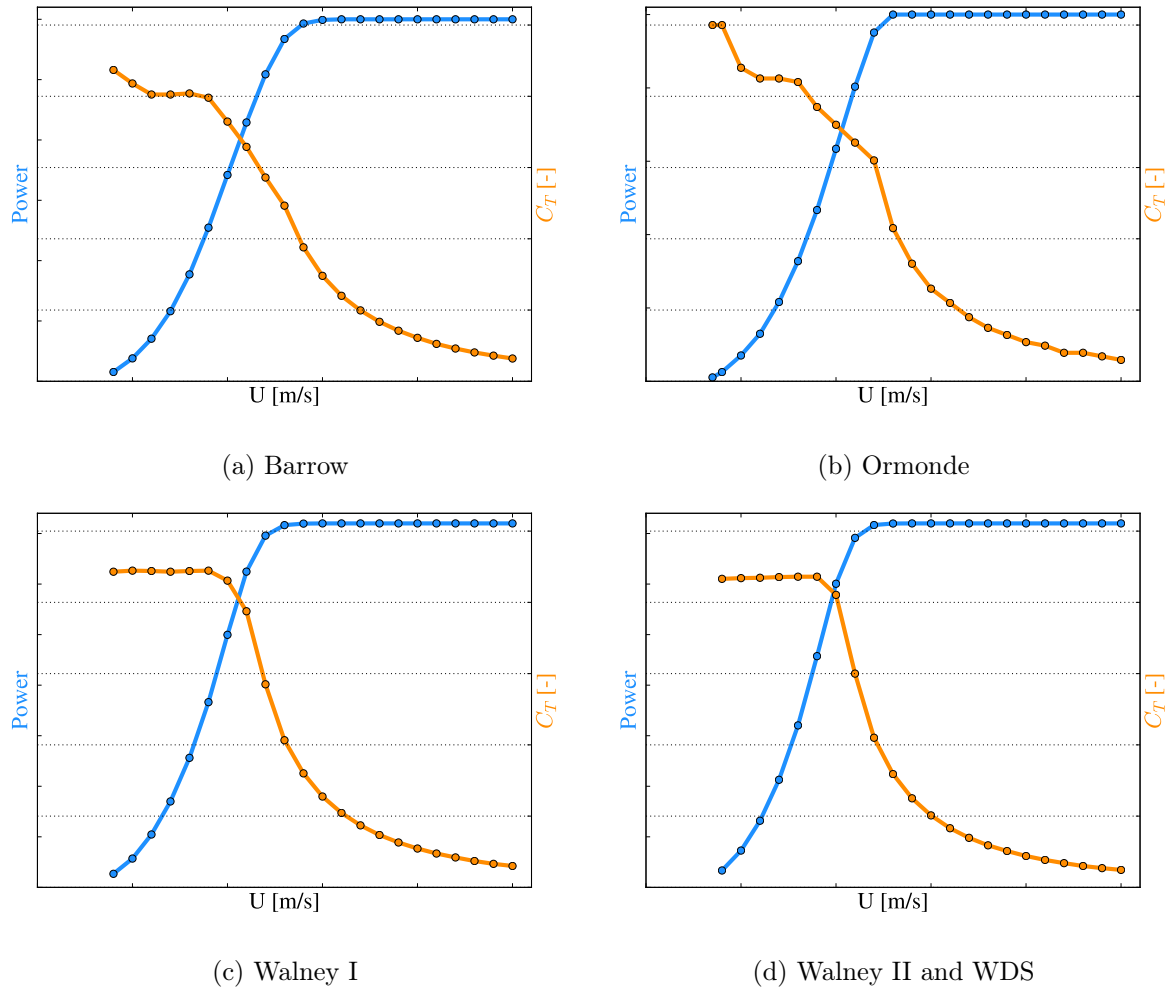


Figure 3.3: Power P and thrust coefficient C_T curves for the turbines in the modeled wind farms

Chapter 4

Methods

The methods utilized to analyze the impacts of horizontal wind speed gradients on AEP estimates are presented in this chapter. First, the chapter offers a few operational definitions before exploring the WRF wind climate of the site based on one year of simulations performed by Poulsen (2019). The next section discusses the wind farm flow models- made up of a wake model and wake summation method. Two of each are examined: the Jensen and Gaussian wake models as well as linear and quadratic wake summation techniques. An overview of PyWake, the Python based modeling tool used for implementing the wind farm flow models, is presented. The next sections outline the five AEP calculation methods used to investigate the impact of wind speed gradients, including how two methods account for both gradients and wakes. A basic estimate for the wake model uncertainty is presented in the final section.

4.1 Definitions

Several definitions core to the analysis are presented in this section. In the case where an AEP estimate is compared with a specified reference value, the percent change is used. The reference value is specified

$$\% \Delta = 100 \frac{N - N_{ref}}{N_{ref}} \quad (4.1)$$

Where $\% \Delta$ is the percent change from the reference N_{ref} to a number N_1 .

Additionally, wind farm efficiency will be defined for this thesis as the ratio of the actual production P_{act} to the reference production P_{ref} .

$$\eta_{wf} = \frac{P_{act}}{P_{ref}} \quad (4.2)$$

4.2 WRF wind climate at the test site

The Weather Research and Forecasting (WRF) model is a mesoscale numerical weather prediction model. A detailed technical description of WRF is provided by Skamarock et al. (2019). Charlotte

B. Hasager et al. (2015) show that WRF is able to predict long term mean wind speeds at several offshore locations by validating simulated wind climates against observed lidar and mast measurements. They find results to be relatively insensitive to several model inputs, but indicate that the choices of boundary layer parametrization and length of the discarded spin-up period have a significant impact on the model prediction.

Poulsen (2019) used the Advanced Research WRF version 3.8.1 to predict the wind climate in the area of a wind farm cluster in the Irish Sea, validating it against SCADA power production data. She examines the effects from neighboring wind farm wakes on Barrow by comparing WRF wind resources predicted by two simulations. The first simulation parametrizes four other wind farms (Ormonde, West of Duddon Sands, Walney I, and Walney) using the EWP (Volker et al. 2015), and the second simulation ignores the presence of the other wind farms. Barrow is not modeled in either simulation. Poulsen (2019) shows that using the EWP in WRF improves the predictions of power production at Barrow compared to ignoring the presence of the other wind farms, even though the EWP underestimates wake losses at that location.

Poulsen (2019)'s WRF simulations cover the period from 00:00:00 on October 1st, 2014 to October 10th, 2015. Her energy yield assessment utilizes one year of data starting the same date. In the simulations she used three nested domains with initial boundary conditions and sea surface temperature from the ERA5 reanalysis and OSTIA, respectively. The outer domain was nudged to the ERA5 reanalysis in the simulations. Simulations were performed with 1 [km] grid spacing in blocks of 11 days with a 24 hour spin-up time, starting at 00:00:00 UTC. Further details about the simulation setup and processing are available in Poulsen (2019).

The WRF simulated wind climates without the wind farm parametrization are assumed to represent the undisturbed wind climate in the region of interest for the present work. Time series of undisturbed wind speeds and directions at the turbine positions and hub heights were extracted from the WRF outputs without the wind farm parameterization. Note that WRF time series are instantaneous snapshots of wind conditions sampled every 30 minutes. WRF outputs through October 5th, 2015 were used to obtain climatologies on a rectangular UTM grid (Zone 30) approximately 26 [km] by 22 [km], covering the area of the wind farms Poulsen (2019) considered. The climatologies include grids of mean wind speed, \bar{U} , Weibull A and k parameters, and sector frequency, f , at levels of 75 [m], 83.5 [m], 90 [m], and 100 [m] for 12 wind direction sectors of 30°. Sector 1 is centered at $0^\circ \pm 15^\circ$. 0° represents flow from the north and positive is clockwise. This is the same format that WAsP uses for wind resource grids, so subsequent references will be to 'WAsP grids.'

Two wind roses are used to visualise the WRF wind resource at the positions and hub heights of turbines BOW-B05 and WOW01-F01. BOW-B05 is located near the center of Barrow and WOW01-F01 is near the center of the cluster. These wind roses are displayed in Figure 4.1.

Figure 4.1 highlights that the wind climate over the cluster area is dominated by winds from the west and southwest. The distribution of wind speeds above 15 [m/s] is also predominantly from the west and southwest at both turbines. Overland winds from the north and northeast (sectors 1-4) are among the least frequent, and have typically lower wind speeds. These sectors are likely to have only a small contribution to the AEP. Note that there is a greater frequency of winds from the north at the hub of WOW01-F01 than BOW-B05.

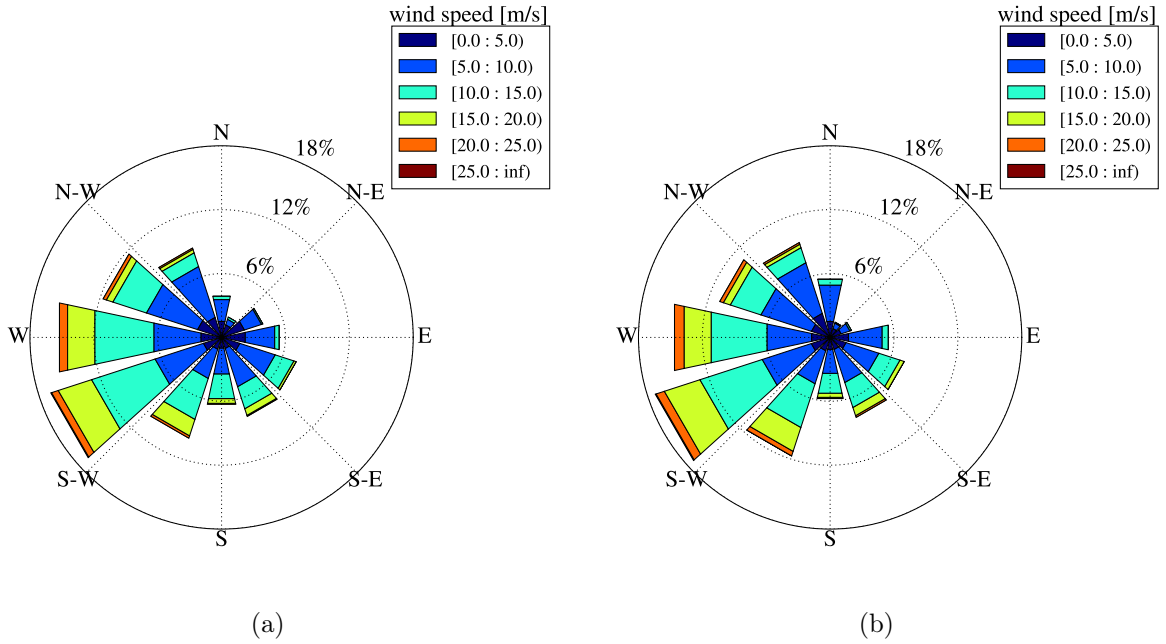


Figure 4.1: WRF simulated wind roses at turbine hub heights for (a) BOW-B05 and (b) WOW01-F01 for the year starting 00:00:00 on October 1st, 2014

To visualize the spatial distribution of mean wind speed, \bar{U} , normalized mean velocity maps are plotted per sector from the $h=75$ [m] wind resource grids in Figure 4.2. \bar{U} at the position of turbine BOW-A07 for each direction sector is used to normalize the map for the corresponding sector. Sectors 1-12 correspond to Subfigures (a)-(l). UTM coordinates are for Zone 30. Similar plots for the remaining heights are displayed in Figures B.1-B.3 in Appendix B.

?? shows the most significant horizontal gradients in normalized mean wind speed in Sectors 1-6 ranging from approximately 15%-30%. Note the lower speeds in the northwest corner of Figure 4.2a. This area is closest to the land, as observed from Figure 3.1b. When the flow is from the north, a strong gradient is observed near the coast, even if the coastline in the WRF simulation does not exactly match the true coastline. Sectors 7-12 show variations of 10% or less over the area covered by the turbines.

4.3 Wind farm flow models

The wind farm flow model consists of an engineering wake model used to describe the propagation of velocity deficit in the wake of one turbine as well as a summation method used to account for the interaction of multiple turbine wakes. The choice of the Jensen wake model as the primary wake model used in the analysis is motivated by the fact that variations of it are frequently used for studying wakes effects in wind farms and for energy yield assessments (Nygaard 2014, Alfredo Peña, K. S. Hansen, et al. 2017, Göçmen et al. 2016). Both the Jensen and Gaussian wake models are implemented in PyWake, so the Gaussian model is used to provide an alternative estimation of the wake losses.

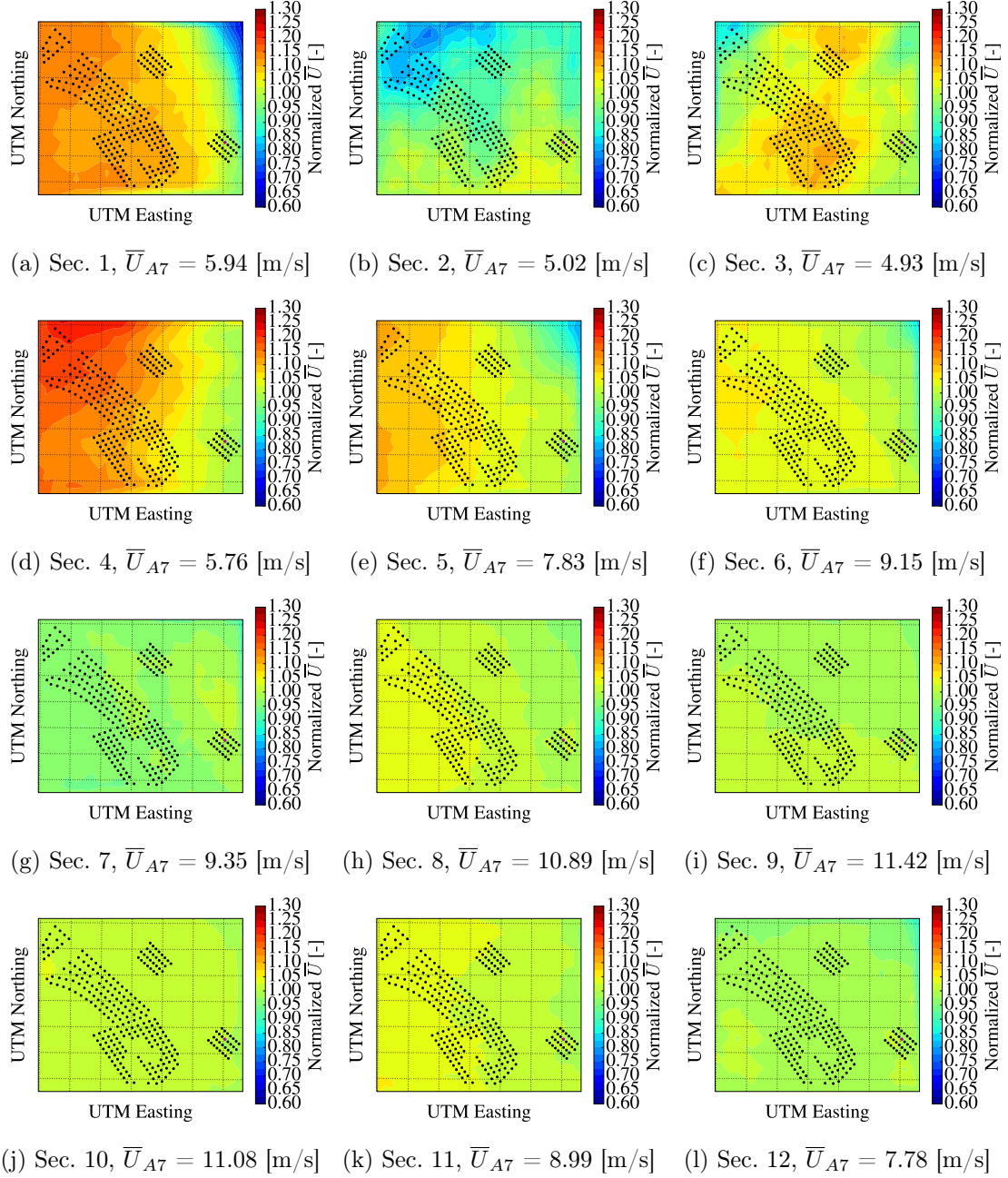


Figure 4.2: Normalized mean WRF wind speeds per wind direction sector at 75 [m]. Bounds of the map area are [456583, 482818] and [5976479, 5998679] in [m] for UTM zone 30 Easting and Northing, respectively. Normalization wind speed presented in the subfigure captions.

4.3.1 Jensen wake model

The Jensen wake model is one of the earliest engineering models for computing velocities in the wake of a wind turbine and stems from the work of N. O. Jensen (1983). The model, based on conservation of mass, describes a single wake which expands linearly with downstream distance from the rotor plane. This expansion is a function of the wake decay coefficient, k . In reality this coefficient depends on factors such as ambient turbulence level and atmospheric stability, but was originally empirically calibrated for the far wake based on measurements Katić, Højstrup,

and N. O. Jensen (1987). A typical value of $k = 0.04$ is frequently used when modelling large offshore wind farms according to Gaumond, P.E. Réthoré, et al. (2012). The velocity in the wake is assumed to be in the form of an axis-symmetric top-hat profile. Turbulence and rotation are neglected. The Jensen model is derived based on the control volume presented in Figure 4.3.

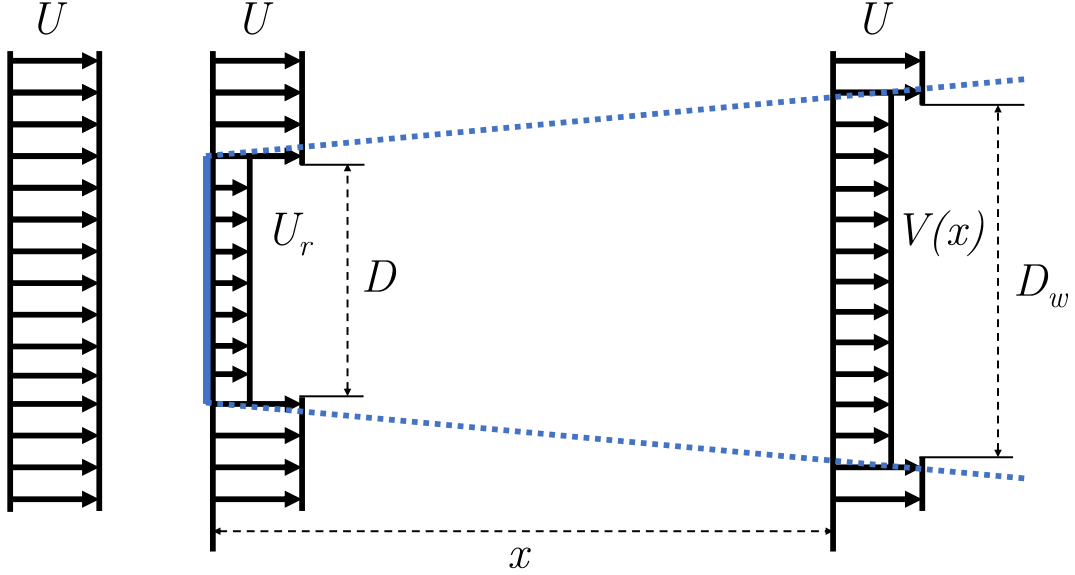


Figure 4.3: Control volume just behind turbine from Katić, Højstrup, and N. O. Jensen (1987) for derivation of Jensen wake model. Rotor plane indicated in with a solid blue line

Of interest is the velocity deficit δU at a downstream position x . This is expressed as

$$\Delta U = U - V(x) \quad (4.3)$$

N. O. Jensen (1983) states that the mass balance over the control volume is given by:

$$D^2 U_r + (D_w^2 - D^2) U = D_w^2 V(x) \quad (4.4)$$

where D is the rotor diameter, U_r is the wind velocity just behind the rotor, U is the free stream wind velocity, and D_w and $V(x)$ are the wake diameter and the velocity at a downstream distance x , respectively.

Assuming linear wake expansion, an ideal rotor (axial induction factor $a=1/3$), and solving for $V(x)$, leads to a wake velocity given by:

$$V(x) = U \left[1 - \frac{2a}{\left(1 + \frac{2kx}{D}\right)^2} \right] \quad (4.5)$$

where a depends on the thrust coefficient C_T ,

$$a = \frac{(1 - \sqrt{1 - C_t})}{2} \quad (4.6)$$

thus the velocity deficit ΔU may be found as a function of downstream distance by:

$$\Delta U = U \left[\frac{(1 - \sqrt{1 - C_T})}{(1 + \frac{2kx}{D})^2} \right] \quad (4.7)$$

Others have built upon the work of N. O. Jensen (1983) by suggesting improvements or new models for wind turbine wakes. The work of Katić, Højstrup, and N. O. Jensen (1987) use a hypothetical mirror image turbine underground to account for wake reflection effects from the ground and also proposed quadratic summation of the velocity deficits of multiple wakes. This results in a model capable of describing flow through a wind farm. This serves as the basis for the Park model, of which multiple variations have been implemented in the wind resource and siting program WAsP as described in Sanderhoff (1993). Alfredo Peña, Pierre Réthoré, and Rathmann (2014) revised the Park model to account for atmospheric stability and turbulence, since these are major factors governing wake recovery. Rathmann et al. (2017) proposed a modified version of the Park model, called Park2, which ensures a consistent physical formulation, uses linear wake superposition, and ignores wake surface reflection.

4.3.2 Gaussian wake model

Bastankhah and Porté-Agel (2014) proposed a different analytical model derived by applying both conservation of mass and momentum, as well as assuming a Gaussian distribution for the velocity deficit in the wake. They suggest that a Gaussian distributed velocity deficit profile was a better choice than the top-hat profile used by the Jensen model because measurements and numerical simulations have shown Gaussian distributions to better resemble far wakes. They also emphasize that top-hat profile based models tend to under and over predict power at the center and edges of wakes, respectively. Linear wake expansion is still assumed in the Gaussian model, and it is also a function of C_T , spatial coordinates, and a wake expansion parameter k^* , which differs from the k in the Jensen model. k^* is the rate of change of the standard deviation of the Gaussian profile with respect to the downstream distance. In Bastankhah and Porté-Agel (2014), values of k^* were obtained from fits with LES data and ranged from 0.023 for to 0.05 for different roughness lengths and turbulence intensities investigated.

Bastankhah and Porté-Agel (2014) derives a Gaussian wake model by first applying conservation of mass and momentum over a different control volume, presented in Figure 4.4. Obtaining the thrust force T in Equation 4.8:

$$T = \rho \int V(x)(U - V(x))dA \quad (4.8)$$

where ρ is the air density, U is the free stream velocity, and A is the area of the control volume, and T is the thrust force experienced by the rotor. Burton et al. (2009) shows that T is also given by:

$$T = 0.5C_T\rho A \quad (4.9)$$

By assuming self similarity in the wake, the velocity deficit can be expressed:

$$\frac{\Delta U}{U} = C(x)e^{-\frac{r^2}{2\sigma^2}} \quad (4.10)$$

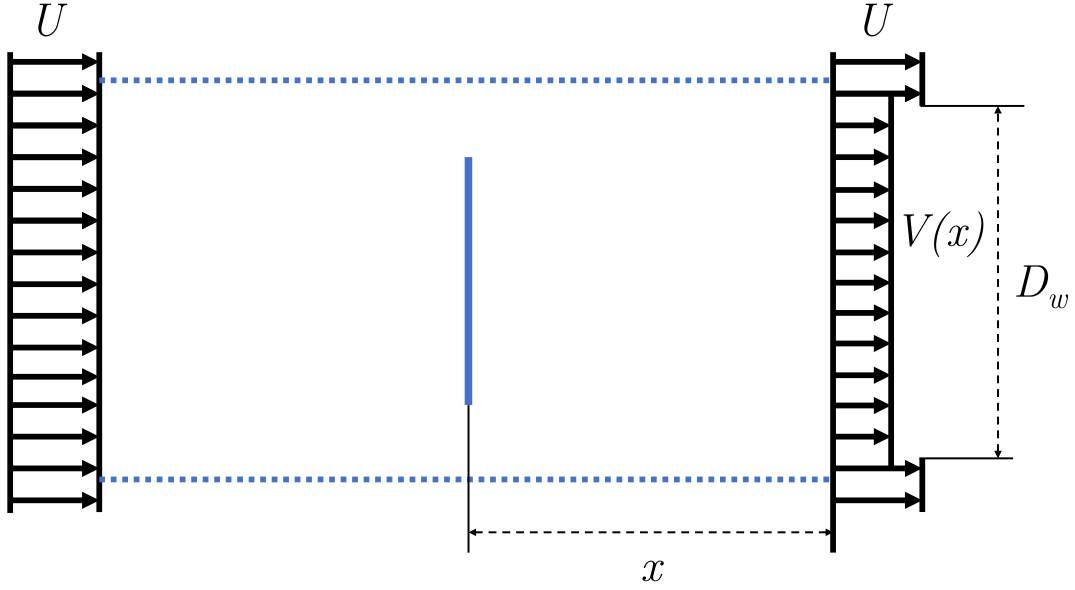


Figure 4.4: Control volume around turbine (Fig. 2b from Bastankhah and Porté-Agel (2014)) for derivation of Gaussian wake model. Rotor plane indicated in with a solid blue line

where $C(x)$ is the maximum normalized wake center velocity deficit at downstream distance x , r is a radial distance from the wake/ rotor center, and σ is the standard deviation of the Gaussian-shaped velocity deficit profile.

Combining Equations 4.8-4.10 and integrating over the area of the control volume from 0 to ∞ :

$$8\left(\frac{\sigma}{D}\right)^2 - 16\left(\frac{\sigma}{D}\right)C(x) + C_T = 0 \quad (4.11)$$

which has one physical solution:

$$C(x) = 1 - \sqrt{1 - \frac{C_T}{8\left(\frac{\sigma}{D}\right)^2}} \quad (4.12)$$

Assuming linear wake expansion:

$$\frac{\sigma}{D} = k^* \frac{x}{D} + \varepsilon \quad (4.13)$$

where

$$k^* = \frac{\partial \sigma}{\partial x} \quad (4.14)$$

and

$$\varepsilon = \lim_{0 \rightarrow \infty} \frac{\sigma}{D} \quad (4.15)$$

or based on LES simulations Bastankhah and Porté-Agel (2014):

$$\varepsilon = 0.2\sqrt{\beta} \quad (4.16)$$

Combining Equations 4.10, 4.12, and 4.13 yields an expression for the velocity deficit in the wake:

$$\Delta U = U \left(1 - \sqrt{1 - \frac{C_T}{8(k^* \frac{x}{D} + \varepsilon)^2}} \right) \exp \left\{ - \frac{1}{2(k^* \frac{x}{D} + \varepsilon)^2} \left(\left(\frac{z - z_h}{D} \right)^2 + \left(\frac{y}{D} \right)^2 \right) \right\} \quad (4.17)$$

4.3.3 Choice of model coefficients

A wake expansion coefficient value of $k = 0.04$ is selected as the baseline value for the Jensen wake model per the recommendation of Gaumond, P.E. Réthoré, et al. (2012). Another value of $k = 0.06$ is also used to provide a sense of the sensitivity of results to this choice. Although k and k^* are distinctly different, the same values are used for k^* in the Gaussian wake model due to the lack of LES simulations to base this choice upon (Bastankhah and Porté-Agel 2014). This makes true comparisons between the results obtained using the Jensen and Gaussian models difficult, but still provides some idea of the results' sensitivity to the choice of wake model and model coefficient.

4.3.4 Wake superposition methods

Several wake superposition techniques have been proposed to account for interaction of multiple wakes. Four of the most common: geometric, linear, quadratic, energy balance wake summation methods are summarized in Göçmen et al. (2016). Combining a wake model and a superposition method allows for modeling of groups of wind turbines (Katić, Højstrup, and N. O. Jensen 1987). Sometimes model results are computed using more than one summation technique to better understand how this choice influences the result, as in Alfredo Peña, K. S. Hansen, et al. (2017). Göçmen et al. (2016) indicates that linear and quadratic wake summation techniques have given good results for offshore wind farms. Both are presented and since they are implemented in PyWake, but only the linear summation method was used in the analysis since this is what Poulsen (2019) used in their energy yield assessment of Barrow.

Renkema (2007) outlines how velocity deficits of multiple wakes can be summed quadratically:

$$\left(1 - \frac{U_i}{U} \right)^2 = \sum_o \left(1 - \frac{U_{io}}{u_o} \right)^2 \quad (4.18)$$

and linearly:

$$\left(1 - \frac{U_i}{U} \right) = \sum_o \left(1 - \frac{u_{io}}{u_o} \right) \quad (4.19)$$

where U_i is the wind speed at turbine i and U_{io} is the wind speed at turbine i due to wake effects from turbine o . The summation covers o upstream turbines from turbine i .

4.4 PyWake

PyWake is an open source collection of engineering wake models implemented in Python for wind farm AEP calculations. It is intended to be computationally fast, suitable for layout optimization, and support complex terrain DTU (2019). PyWake is primarily developed by DTU Wind Energy, and official releases are available through the Python Software Foundation.

PyWake was selected for this analysis because of the ability to utilize different engineering wake models for computationally fast wake flow cases calculations as well as the ability to use

wind resource data of different formats. The Jensen and Gaussian wake models implemented in PyWake have been validated against measurements, LES, and RANS simulations for both single wake cases and wind farms in Energy (2019). These two models (explained in detail below) are utilized in this thesis because of their ready implementation in PyWake.

PyWake has the ability to calculate local effective wind velocities and turbine powers for individual flow cases as well as AEP for a site. An AEP calculation in PyWake involves defining a wind farm model by selecting a wake model, defining model coefficients, and selecting a wake summation method. Additional site and turbine characteristics are required including turbine positions, wind climate, site topography, turbine thrust coefficient and power curves, hub heights, and rotor diameters. A flowchart highlighting the exchange of information within the PyWake wind farm model for an AEP calculation is presented in Figure 4.5.

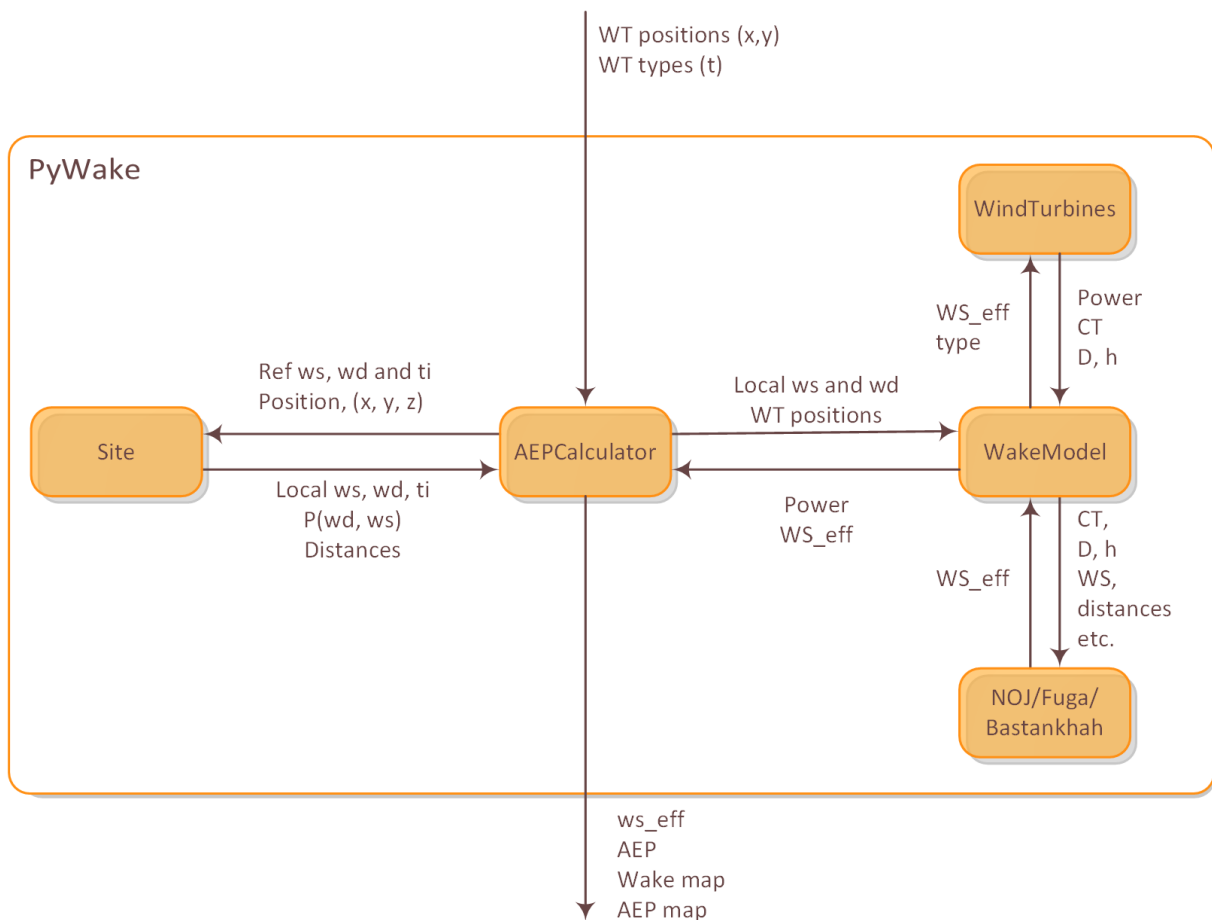


Figure 4.5: PyWake AEP calculation flowchart from PyWake documentation (DTU 2019)

Once the wind farm model is defined, an AEP calculation in PyWake involves computing the local effective wind speed and power at each turbine position over a range of inflow cases defined by wind speeds and directions. These ranges typically cover wind speeds from 4 to 25 [m/s] (in 1 [m/s] bins) and wind directions from 0° to 360° (in 1° bins), per the recommendation of Feng and Shen (2015). The calculation of effective wind speeds necessitates determining the downstream order of turbines, computing turbine distances, velocity deficits in wakes, and accounting for multiple wakes through the wake summation technique of choice. The calculation then takes into

account the probability of each flow case based on the wind resource, and is used to calculate the the likely energy contribution from each flow case, as well as the total AEP.

4.5 AEP calculation methods

The present work employs five different AEP calculation methods to investigate the impact of wind speed gradients in a wind farm cluster. Once a wake model and wake summation method are selected, each of these calculation methods is implemented using PyWake. While all of these methods follow the principle outlined in Equation 2.1, choices about wind resource data format, consideration of wind speed gradients, and inflow definition for wake models lead to differences in implementation. To clarify the differences between the methods, a naming convention is highlighted in Figure 4.6. A summary of each calculation procedure is presented in the following subsections.

The first distinction made between calculation methods is the format of the wind resource input data. As described in section 4.2, WRF simulated free stream wind conditions are available either as time series interpolated to the turbine hub positions or as rectangular wind resource grids mirroring the format of wind resource grids used in WAsP. Three of the calculation methods utilize time series data, and are hence referred to as 'time series based' or 'time series methods' (TSM). The remaining two methods are referred to as 'WAsP grid based' or 'WAsP grid methods' (WGM). Note that the WAsP grid functionality in PyWake is not yet available through official releases and has not been fully validated.

The second difference in the calculation methods stems from the choice of how to define the inflow to the wake model. The methods are further broken into two categories: those which assume homogeneous inflow to the wake models and attempt to define it in a representative manner, and those methods which account for spatial gradients in wind conditions. These are referred to as 'homogeneous' (H) and 'gradient' (G) methods.

The last distinction indicates which positions are used in the definition of the inflow to the engineering wake models. The wind conditions used are taken either from a single point or from all turbine positions - indicated in the method name by the words 'point' and 'all', respectively. The implementation of each calculation method used- G.all WGM, H.point WGM, G.all TSM, H.point TSM, and H.all TSM- is discussed below.

4.5.1 Time series based methods

The desired outcome of the time series based methods are time series of turbine powers which can be used to calculate the energy production over the interval of the wind resource time series. Effective wind speeds and turbine powers at each time step are computed based on the selected wake model, model coefficients, and summation method. An energy production estimate is obtained by assuming that the power production is constant over each time step. Time series based AEP calculation methods utilize one year of data covering 1st October, 2014 to 30th September, 2015, the same period utilized for the wind resource assessment in Poulsen (2019).

Since the Jensen and Gaussian engineering wake models make the assumption of homogeneous free stream flow through the domain (spatial uniformity in wind speed and direction), the H.point and H.all methods attempt to derive representative homogeneous inflow conditions for the site

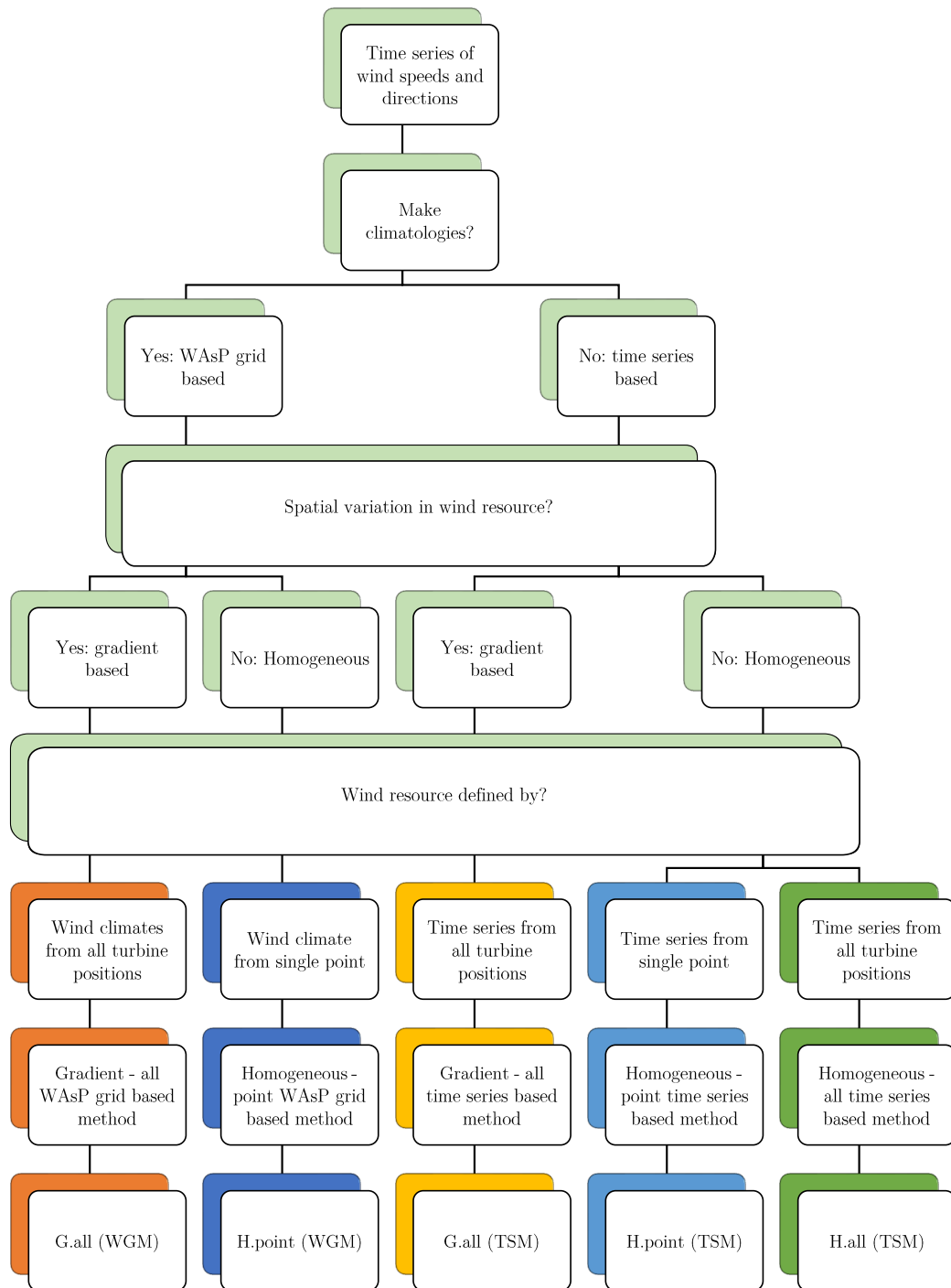


Figure 4.6: Flowchart depicting naming procedure for the five methods used in the AEP calculation

and time step in question. The G.all method attempts to overcome the challenge of how to couple effects of turbine wakes and wind speed gradients without changing the underlying wake models. It does this by averaging turbine powers at all time step flow conditions rather than averaging the flow conditions to calculate powers. The time series methods are further explained below.

H.point time series method

The H.point method assumes that the wind climate of a single point approximates the average wind climate over the site of interest. For each time step the inflow to the wake model is assumed homogeneous over the site and equal to the wind conditions of the selected reference point. Time step turbine powers are computed based on the effective wind speed at each turbine position due to wake effects. Note that the selection of the reference point has a significant impact on the result if the average wind climate of the site deviates from that of the selected point. Let the power of wind turbine i and time step j be represented as P_{ij} . This power is a function of the effective wind speed at the turbine position and time step, e_{ij} , resulting from the velocity deficits predicted by the wake model due to inflow wind speed U and direction θ in [deg]. Using the H.point method, P_{ij} can be expressed as a function of the wind conditions at a reference point, $U_{point,j}$ and $\theta_{point,j}$ at time step j :

$$P_{ij}(e_{ij}(U_{point,j}, \theta_{point,j})) \quad (4.20)$$

The total power of a wind farm at time step j using the H.point method is given by:

$$P_{tot,j} = \sum_{i=1}^N P_{ij}(e_{ij}(U_{point,j}, \theta_{point,j})) \quad (4.21)$$

where N is the total number of wind turbines considered in the calculation.

H.all time series method

The H.all time series method attempts to define a representative homogeneous flow case for each time step at the site. This is done by vector averaging the time step free-stream wind velocities from all turbine positions to serve as the input to the wake model. Let the m^{th} wind velocity vector in a set of N velocities be defined by wind speed U_m and direction θ_m in [deg]. To compute the vector average of the set, components are determined based on the wind speed magnitude and wind direction in [rad], ϕ_m , which is given by:

$$\phi_m = \theta_m \frac{\pi}{180} \quad (4.22)$$

Then the components in the stream-wise and crosswind directions, u_m and v_m respectively, are computed as:

$$u_m = -|U_m| \cos(\phi_m) \quad (4.23)$$

$$v_m = -|U_m| \sin(\phi_m) \quad (4.24)$$

The average wind speed magnitude, \bar{U}_j , over the set of N velocities occurring at time step j is found by taking the mean of the magnitudes of the components.

$$\bar{U}_j = \frac{1}{N} \sum_{m=1}^N \sqrt{u_m^2 + v_m^2} \quad (4.25)$$

When computing the average wind direction from a set of wind velocities, a unit vector average is employed because an arithmetic mean would leave the average wind direction ill-defined. The unit vector components in the stream-wise and crosswise directions, V_x and V_y respectively, are calculated without weighting by wind component magnitude:

$$V_{x,m} = -\cos(\phi_m) \quad (4.26)$$

$$V_{y,m} = -\sin(\phi_m) \quad (4.27)$$

The respective means of the unit vector components are computed:

$$\bar{V}_x = \frac{1}{N} \sum_{m=1}^N V_{x,m} \quad (4.28)$$

$$\bar{V}_y = \frac{1}{N} \sum_{m=1}^N V_{y,m} \quad (4.29)$$

And then the average wind direction in degrees, $\bar{\theta}$ is computed as:

$$\bar{\theta} = \frac{180}{\pi} \arctan \frac{\bar{V}_y}{\bar{V}_x} + \Theta \quad (4.30)$$

where Θ is a constant angle of 180° . Note that when implemented in Python, the command `arctan2(y,x)` from the Numpy package computes the element-wise arc tangent of y/x and chooses the correct quadrant.

The total wind farm power as predicted by the H.all time series method is given by:

$$P_{tot,j} = \sum_{i=1}^N P_{ij}(e_{ij}(\bar{U}_j, \bar{\theta}_j)) \quad (4.31)$$

G.all time series method

The G.all time series method accounts for wind speed and direction gradients across the site. For each time step it assumes that the power produced by each turbine is the average of the powers produced at that turbine across each of the flow cases corresponding to flow conditions at each turbine position. For a group of 270 wind turbines, this corresponds to taking the mean power at each turbine across 270 homogeneous - point method cases, at each time step.

This process is illustrated mathematically. The power produced at turbine i and time step j according to the G.all time series method is as follows:

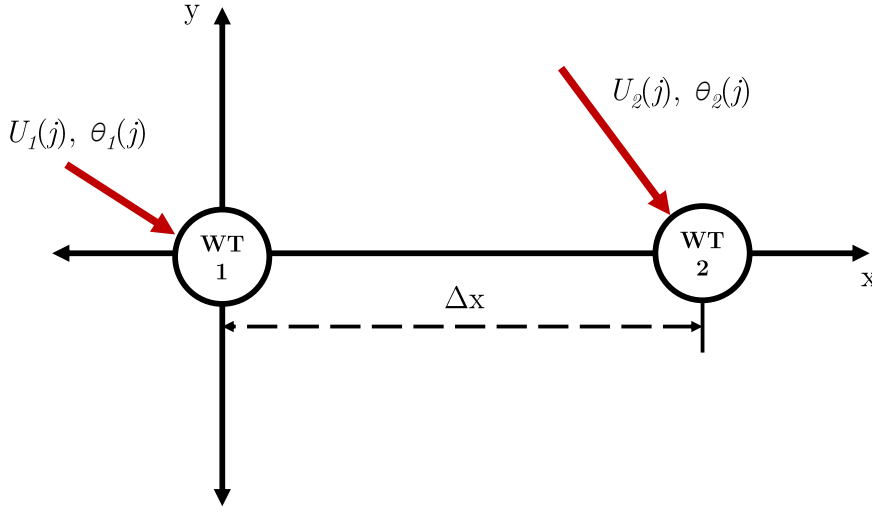


Figure 4.7: Graphic depicting a simple two turbine wind farm for illustrating the methods

$$P_{ij} = \frac{1}{N} \sum_{i=1}^N P(e_i(U_{ij}, \theta_{ij})) \quad (4.32)$$

The G.all total wind farm power at time step j , $P_{tot,j}$, is given by:

$$P_{tot,j} = \sum_{i=1}^N P_{ij} \quad (4.33)$$

On a Lenovo Yoga 720 with an Intel Core i7 processor, it takes approximately 0.06 seconds to compute the effective wind speeds and powers for 270 wind turbines using PyWake for a flow case of a single wind speed and direction. Computing 270 flow cases is required for each time step with the G.all time series method. Assuming a time step interval of 30 minutes in the wind resource data, calculating the annual energy production based on 17,520 time steps would take approximately 79 hours. Since this is impractical, the DTU High Performance Computer cluster was employed for the time series based calculations. The time series was split up into 20 blocks to be computed on different processors in parallel, reducing the computational time to approximately 10 hours.

A simplified case

To illustrate the differences between the time series based calculation methods clearly, a simple case is defined. Imagine a simple wind farm consisting of two wind turbines (WT 1 and WT 2) spaced a distance Δx apart- shown in Figure 4.7. The velocity vector for wind turbine 1 (WT 1) at time step j is given by the wind speed U_{1j} and wind direction θ_{1j} in [deg]. The values at WT 2 are similarly defined.

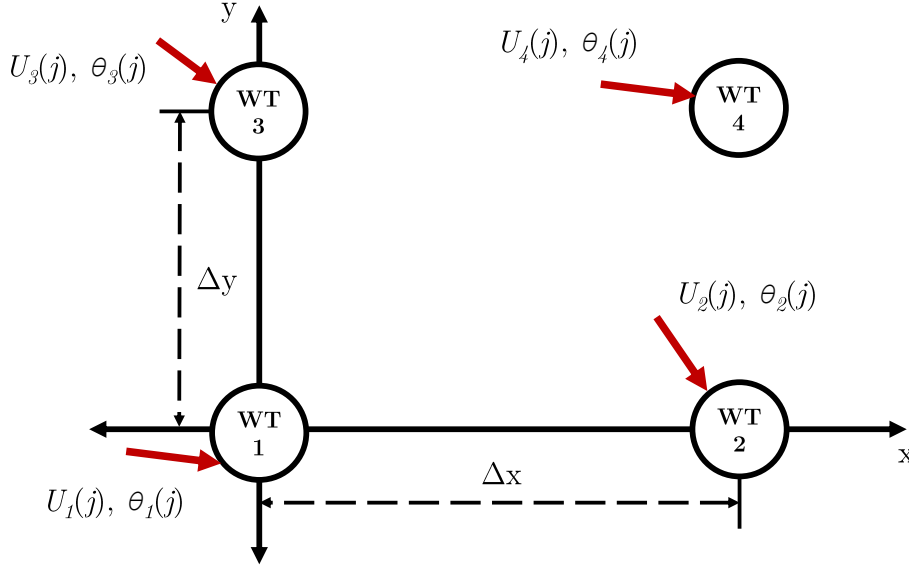


Figure 4.8: Illustration of four turbine verification case with $\Delta x = \Delta y = 1000$ [m]

The total wind farm powers produced $P_{tot,j}$, as predicted by each of the time series methods are summarized in Equations 4.34 - 4.36 below. Let the reference point for the H.point methods be the position of WT 2.

H.point total power

$$P_{tot,j} = P_{1j}(e_{1j}(U_{2j}, \theta_{2j})) + P_{2j}(e_{2j}(U_{2j}, \theta_{2j})) \quad (4.34)$$

H.all total power

$$P_{tot,j} = P_{1j}(e_{1j}(\bar{U}_j, \bar{\theta}_j)) + P_{2j}(e_{2j}(\bar{U}_j, \bar{\theta}_j)) \quad (4.35)$$

G.all total power

$$P_{tot,j} = \frac{P_{1j}(e_{1j}(U_{1j}, \theta_{1j})) + P_{1j}(e_{1j}(U_{2j}, \theta_{2j}))}{2} + \frac{P_{2j}(e_{2j}(U_{1j}, \theta_{1j})) + P_{2j}(e_{2j}(U_{2j}, \theta_{2j}))}{2} \quad (4.36)$$

Verification case

To verify that the H.all and G.all time series based methods are implemented as intended, a test case is considered. The test case consists of a hypothetical wind farm of four 3.6 [MW] turbines placed at the corners of a square with 1000 [m] side length ($\Delta x = \Delta y$). This is illustrated in Figure 4.8. Hypothetical time series of wind speeds, U_{ij} [m/s], and directions, θ_{ij} [deg], are assigned to each turbine position, i . The values are presented in Table 4.1.

Total wind farm power at each time step, $P_{tot,j}$, for the G.all and H.all methods is presented in 4.9 for the Jensen wake model with $k = 0.04$. The process was repeated for both linear and quadratic wake summation methods, yielding the same result since this wind farm configuration does not lead to a significant number of overlapping wake cases. Note that the difference between

Time	U_1	U_2	U_3	U_4	θ_1	θ_2	θ_3	θ_4
$j = 1$	10	8	8	9	270	279	291	292
$j = 2$	7	2	9	10	180	123	122	182
$j = 3$	9	10	15	20	90	87	26	76

Table 4.1: Hypothetical wind conditions for the verification case

the two methods is most significant in the third time step where both the standard deviation of time step wind speeds and maximum wind speed difference across the wind farm are largest. The effect of wind direction variation depends on the layout since this determines which turbines are waked for a given direction.

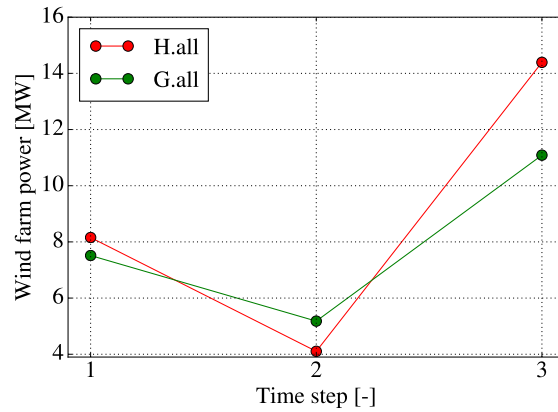


Figure 4.9: Comparison of G.all and H.all calculation approaches for a test case. Values matched the reference.

Results from the implementation of the G.all and H.all methods implemented using PyWake were found to match results obtained with the Matlab implementation from Alfredo Peña, K. S. Hansen, et al. (2017). When using PyWake it is important that the user be aware of interpolation/extrapolation of the power (P) curve and thrust coefficient (C_T) curve. The corners of the power curves and thrust coefficient curves at the cut-in, U_{cut-in} , and cut-out, $U_{cut-out}$, wind speeds were defined to the nearest thousandth of one [m/s].

4.5.2 WAsP grid based methods

The WAsP grid methods use wind resource distributions at each turbine position to calculate AEP based on Equation 4.37. P_{ilk} is the power at wind turbine i due to the effective wind speed e_{ilk} predicted by the wake model with inflow conditions defined by the k^{th} inflow wind speed U and l^{th} wind direction θ . p_{ilk} is the probability of those inflow conditions occurring at the position of turbine i .

$$AEP = 8760 \sum_{i=1}^N \sum_{l=1}^L \sum_{k=1}^K P_{ilk} p_{ilk} \quad (4.37)$$

where N is the number of turbines, K is the number of wind speeds, and L is the number of wind directions. p_{ilk} can be thought of as the product of the individual probabilities of the inflow

wind speed p_U and wind direction p_θ .

$$p_{ilk} = p_U p_\theta \quad (4.38)$$

Since the statistics are per wind direction sector, the probability of the wind direction is taken to be the product of the sector frequency f and the wind direction bin width, $\Delta\theta$.

$$p_\theta = f_\theta \Delta\theta \quad (4.39)$$

The probability of a wind speed falling in the wind speed bin centered at $U \pm \Delta U$ is given by:

$$p_U = p(U_i - 0.5\Delta U < U_i \leq U_i + 0.5\Delta U) \quad (4.40)$$

This value is obtained using a cumulative distribution function (CDF). Generally a CDF represents the probability of a value occurring which is less than or equal to certain value.

$$F_x(U) = p(U \leq u) \quad (4.41)$$

This can be used to find the probability of occurrence between two values a and b :

$$p(a < U \leq b) = F_x(b) - F_x(a) \quad (4.42)$$

When Weibull distribution is assumed, its corresponding CDF is as follows:

$$F_x(U; k, A) = 1 - e^{-(U/A)^k} \quad (4.43)$$

and this is utilized to compute p_U . The interpolating method for sector-wise Weibull distributions and joint distribution of wind speed and wind direction is implemented in PyWake based on Feng and Shen (2015). In order to compute this probability, the Weibull scale (A), shape (k) parameters, and wind direction sector frequency, f , are linearly interpolated in two dimensions to the turbine positions from the resource grids. In a situation where the turbine hub height falls between heights of extracted grid files, as shown in Figure 4.10, the value must then be interpolated to the hub height.

In the figure, a turbine hub is shown between grid levels and so the wind climate must be interpolated. The main distinction between the H.point and G.all WAsP grid methods lies in the layout of the resource grids; one assumes a homogeneous wind distribution across the site while the other accounts for local variation in this distribution.

H.point WAsP grid method

As in the case of the time series based H.point method, the WAsP grid based H.point method assumes that the wind climate of a reference point approximates the wind climate of the site. The input grid files are homogeneous, reflecting the wind climate of the reference point.

G.all WAsP grid method

The G.all WAsP grid method accounts for spatial variation in the wind resource via spatial grids of the statistical parameters defining this locally varying resource. The way that the gradients are coupled with the wake models in this case effectively amounts to a post processing step - in the multiplication of probabilities.

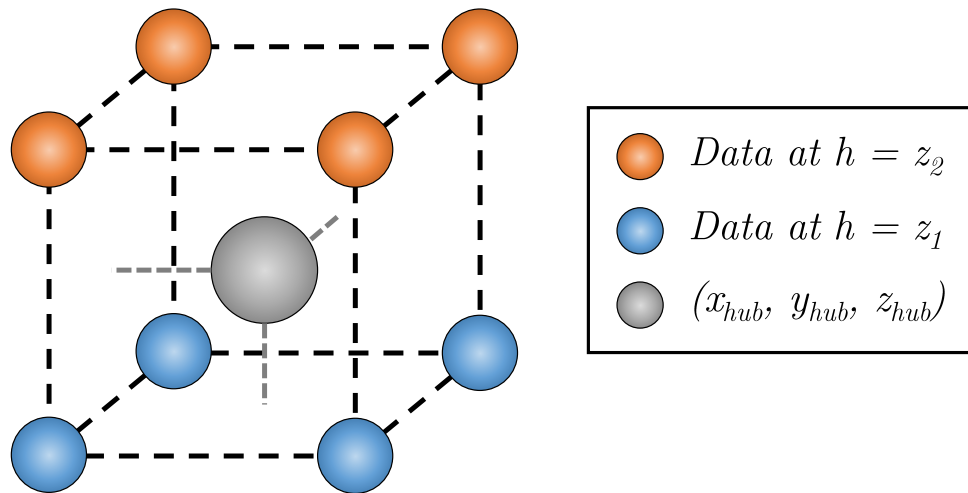


Figure 4.10: Illustration highlighting need for interpolation between wind resource grid levels

4.6 Wake free reference power

Wake effects and the effects of modeling the whole cluster are made more clear by examining wind farm efficiency, or the ratio of AEP computed with wake effects to a wake-free reference AEP. The calculation of the wake-free reference AEP is as follows.

4.6.1 Time series based wake-free reference power

The time series wake-free reference AEP is computed from a time series of wake-free reference powers. A reference power for each turbine is computed at each time step with each AEP calculation method described above based on the undisturbed local wind speeds based from the WRF time series. This is summarized:

1. G.all
 - (a) For each time step look up each turbine's power at the free stream wind speed conditions of each turbine in the analysis
 - (b) Average each turbine's powers across all wind conditions occurring at the time step to obtain wake-free reference power
2. H.all
 - (a) For each time step compute the representative wind speed based on vector averaged free stream wind conditions from each turbine
 - (b) Look up the power of each turbine at the representative wind speed to obtain wake-free reference power
3. H.point

- (a) For each time step get free stream wind conditions at a single point (position of turbine BOW-B05, for example)
- (b) Look up each turbine's power at that wind speed to obtain wake-free reference power

4.6.2 WAsP grid based wake-free reference power

The wake-free reference powers for the WAsP grid methods are computed in the same way as AEP, but the wind speed at each turbine corresponds to the inflow wind conditions.

4.7 Model uncertainty

In a case where no measurements are available and the wind resource is obtained with mesoscale models such as WRF, Henderson et al. (2014) suggest an overall AEP uncertainty of 7.5%, even indicating it may be too generous. This example highlights how uncertainty in AEP estimates represents a challenge for the wind energy industry. Improvements across disciplines can help to reduce overall AEP uncertainty. Although there are a number of contributing factors to uncertainty in the present AEP calculations, the focus of the thesis is on accounting for wind speed gradients and wake effects. Therefore the primary investigation of uncertainty is taken to be the wake model uncertainty. Nygaard (2015) argues that a 15% of the predicted wake loss represents a conservative uncertainty for the Jensen wake model.

To estimate the wake model uncertainty, u_{wm} as a percentage of the AEP, the following equation is used:

$$u_{wm} = \frac{.15(AEP_{wakefree} - AEP)}{AEP} \quad (4.44)$$

Chapter 5

Results

This chapter first presents a simplified case which is used to clarify the differences between each of the time series based calculation methods. Next, each of the five calculation methods is used to estimate the AEP at a single wind farm from the test site. Results are compared to see if the methods accounting for wind speed gradients yield difference compared with the homogeneous methods. The overall wind farm efficiency is discussed in the context of internal and external wake effects. These analyses are extended to the AEP estimates for the entire wind farm cluster. The overall implications of the results are discussed in the context of wake model uncertainty in the last section.

5.1 A simplified case

The simplified case described in section 4.5.1 is investigated to illustrate how the time series based calculation methods work. Refer to the illustration of the two turbine wind farm in Figure 4.7. The Jensen wake model with linear wake summation and a model coefficient of $k = 0.04$ is used for this analysis. Note that the phrase 'with respect to' is abbreviated as 'w.r.t.' in several figures below.

For a given time step the wind speed difference between the two turbine positions ΔU is given by:

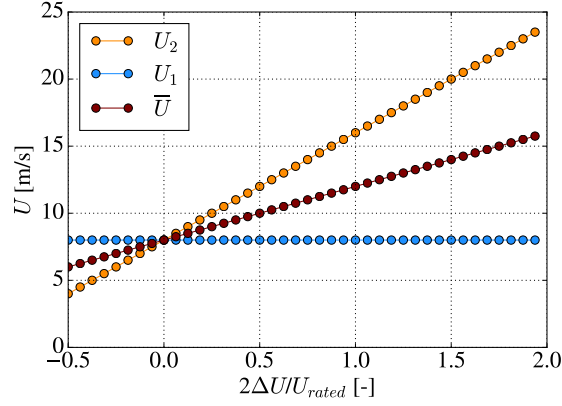
$$\Delta U = U_2 - U_1 \quad (5.1)$$

and Δx is the distance between the turbines:

$$\Delta x = x_2 - x_1 \quad (5.2)$$

Let U_1 at the hub height be fixed at half of the rated wind speed U_{rated} , corresponding to 8 [m/s] for the Vestas V90 from Barrow. If U_2 varies such that the nondimensional wind speed difference $\frac{2\Delta U}{U_{rated}}$ is between -0.5 and 2, then the values of U_2 span the majority of the power curve (4 to 24 [m/s]). These wind speed ranges are specified in Figure 5.1 along with the mean, \bar{U} , for each value of $\frac{2\Delta U}{U_{rated}}$.

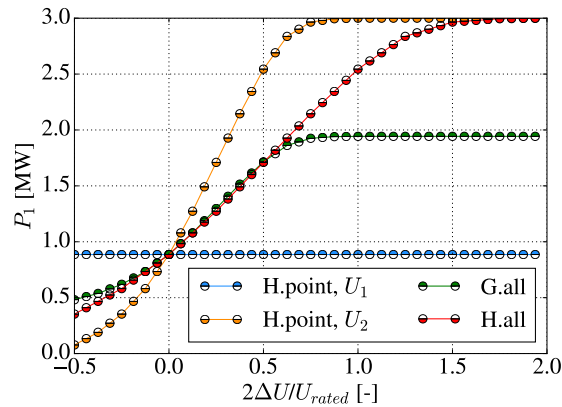
Variation in wind direction across the site is not considered in the simplified case.

Figure 5.1: Wind speeds for range of $\frac{2\Delta U}{U_{rated}}$

5.1.1 Flow direction 1: wake free conditions ($\theta = 0^\circ$)

A wake free flow direction is considered ($\theta_1 = \theta_2 = 0^\circ$) for the wind speeds described above. The turbine used is the Vestas V90 turbine from Barrow. The powers predicted at each turbine in this case are independent of turbine spacing, meaning that the impact of the velocity difference (rather than gradient) between the turbines is the focus.

Each of the methods can be explained by examining the powers they predict at at WT 1 (P_1) for the above scenario, shown in Figure 5.2. H.point predicts P_1 based on a flow case defined by the reference point. G.all predicts P_1 as the mean power produced by WT 1 across flow cases from all the wind conditions at the turbine positions. This amounts to averaging two flow cases, $P_1(U_1)$ and $P_1(U_2)$. Since H.all predicts turbine power based on a flow case defined by \bar{U} , P_1 falls between the H.point predictions. Once \bar{U} reaches U_{rated} , the H.all P_1 also reaches P_{rated} . This is visible in Figure 5.2 when $\frac{2\Delta U}{U_{rated}} = 1.5$. This exercise illustrates that each method builds its prediction based on one or more component wake model flow cases.

Figure 5.2: P_1 vs. $\frac{2\Delta U}{U_{rated}}$

Each method predicts a different value of P_1 for nonzero wind speed differences. Each method also predicts that $P_1 = P_2$ since the lack of wake effects ensures they are the same in each

component flow case. At a single time step this means that Equations 4.34 - 4.36 for total wind farm power P_{tot} can be simplified to Equations 5.3 - 5.5, shown below:

H.point total power:

$$P_{tot} = 2P(U_{point}) \quad (5.3)$$

H.all total power:

$$P_{tot} = 2P(\bar{U}) \quad (5.4)$$

G.all total power:

$$P_{tot} = P(U_1) + P(U_2) \quad (5.5)$$

Figure 5.3 shows this is true as P_{tot} is twice P_1 for each method. H.point takes WT 2 as the reference.

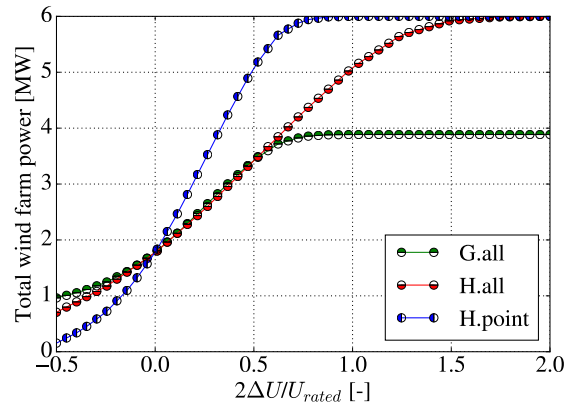


Figure 5.3: Total wind farm power, P_{tot} predicted by the different methods

Since the wind speeds at the turbine positions are prescribed and there are no wake effects, the true wind farm power can be calculated as the sum of the turbine powers at their respective wind speeds. For this wake free situation, this exactly corresponds to the power predicted by G.all in Equation 5.5. The percent changes of P_{tot} relative to the true power are presented for each method in Figure 5.4.

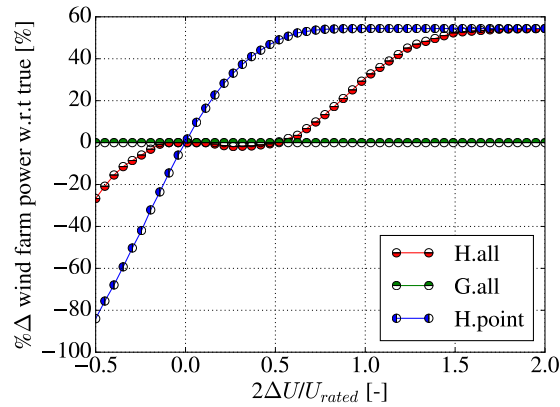


Figure 5.4: $\% \Delta$ in total wind farm power w.r.t true for the different methods

Figure 5.4 shows that all three methods predict similar values P_{tot} for small ΔU . The G.all method predicts the true value of P_{tot} across all values of ΔU . The H.all method is able to represent the true power for small ΔU , but fails to capture the true power, except at two points. As the absolute value of ΔU grows, the quality of the homogeneous assumption declines, leading to errors for the H.point and H.all methods with respect to the true P_{tot} . Errors for the H.all method are less than 3% between approximately $\frac{2\Delta U}{U_{rated}} = -0.17$ and 0.6.

The quality of the H.point assumption of a homogeneous U depends on the selected reference point. Taking the reference at the midpoint between the turbines would be equivalent to the H.all method, which represents an improvement over taking WT 2 as the reference point, but only predicts the true power at two points. This stems from the fact that, except for certain values, the cube of the mean of some numbers (say U_1 , U_2 , and U_i) is not the same as the mean of the cubes of those numbers:

$$\left(\frac{U_1 + U_2 + U_i}{3}\right)^3 \neq \frac{U_1^3 + U_2^3 + U_i^3}{3} \quad (5.6)$$

When U_1 , U_2 , and c are such that Equation 5.6 does not hold, the H.all and G.all methods should yield the same prediction. This is the case for a zero wind speed difference. A portion of the turbine power curve represents a cubic function, explaining the difference between the H.all and G.all methods. This is confirmed by repeating the same exercise, but replacing the power curve with a linear function: $P(U) = 150U - 600$. In this instance the H.all method is able to predict the true power exactly, showing no difference with G.all. This is due to the fact that

$$C\left(\frac{U_1 + U_2 + U_i}{3}\right) = \frac{U_1C + U_2C + U_iC}{3} \quad (5.7)$$

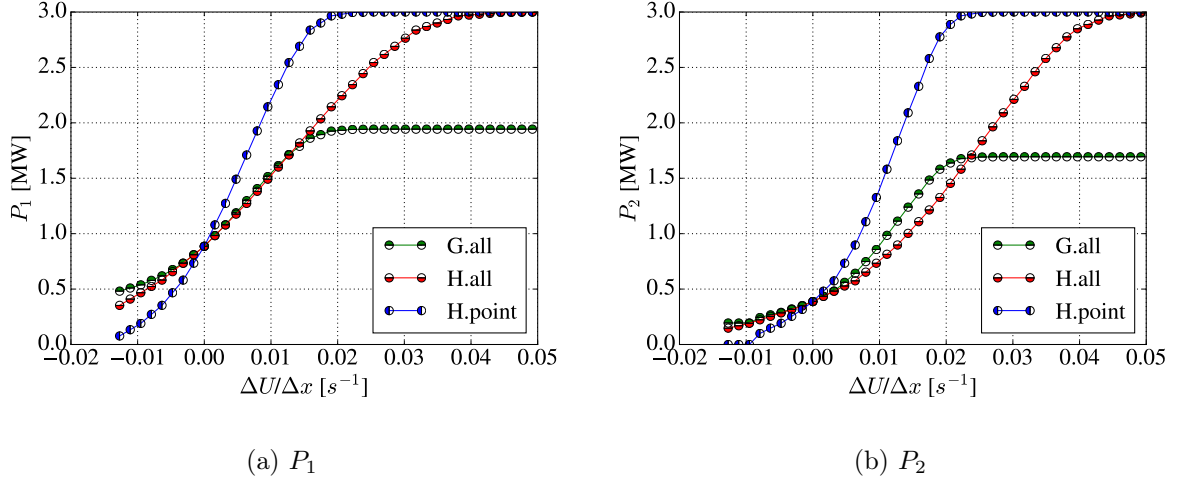
where C is a constant, and U_1 , U_2 , and U_i are only raised to the first power. This explains why for a realistic power curve the H.point method error approaches a limiting value when \bar{U} approaches the U_{rated} . The power curve is linear above U_{rated} .

5.1.2 Flow direction 2: WT 2 waked ($\theta = 270^\circ$)

Analysis for a situation where WT 2 is in the wake of WT 1 is considered in order to represent more of the variables influencing AEP in a real wind farm cluster. Now that WT 2 is in a wake, P_2 is a function of the effective wind speed at position 2, e_2 . If U_1 and U_2 represent undisturbed flow conditions at the turbine positions (derived from WRF for example), then e_2 needs to be modeled.

The velocity deficit predicted by the Jensen wake model depends on C_T curve and the downstream distance turbine spacing, influencing the total wind farm power predicted by the different methods. Since turbine spacing matters, wind speed gradients ($\frac{\Delta U}{\Delta x}$) are considered rather than wind speed differences (ΔU). ΔU is the difference in the undisturbed conditions. Turbine powers P_1 and P_2 predicted by all three methods are displayed in Figure 5.5 for $\Delta x = 7D$, where D is the rotor diameter.

Figure 5.5 underscores the impact of the wake effects. Comparing Figures 5.5a and 5.5b reveals that $P_1 \neq P_2$ for since the e_2 lower than the free stream conditions. Figure 5.5b indicates that H.point method predicts no power production from P_2 when $\frac{\Delta U}{\Delta x}$ is sufficiently negative because $e_2 < U_{cut-in}$. The effects from this are less pronounced in the G.all and H.all powers.

Figure 5.5: Turbine powers (a) P_1 and (b) P_2 predicted by the different methods for $\Delta x = 7D$

To better illustrate the impact of turbine spacing, the powers at each turbine as predicted by the G.all method for $\Delta x = 5D$, $7D$, and $9D$ are plotted in Figure 5.6a. Since the true power is not precisely known in the waked case, the $\% \Delta$ of the H.all prediction with respect to the G.all predictions are shown in Figure 5.6b for the same values of spacing.

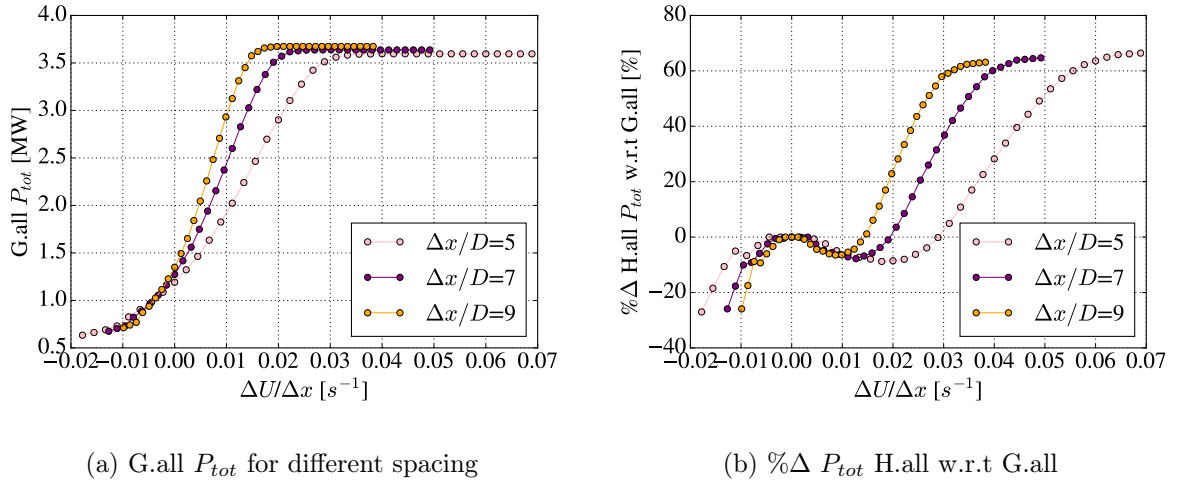


Figure 5.6: Effect of gradients and turbine spacing in the waked situation

As observed in Figure 5.6a, P_{tot} predicted by G.all decreases with the turbine spacing due to increased wake losses. Notice the curves for different spacing do cross at a nonzero value of $\frac{\Delta U}{\Delta x}$ due to the wake effects. The shape of the curves for the most negative values of $\frac{\Delta U}{\Delta x}$ shows effects from the cut-in of WT 2. These effects are also observable for negative $\frac{\Delta U}{\Delta x}$ as small dips in the curves showing the $\% \Delta$ between the H.all and G.all predictions in Equation 4.1. The troughs in the curves present for positive $\frac{\Delta U}{\Delta x}$ stem from the under-prediction of H.all relative to G.all in part of the cubic portion of the power curve which is observable in Figure 5.5.

5.2 Barrow AEP

The five AEP calculation methods are used to investigate the impact of accounting for wind speed gradients in AEP estimates for a single wind farm. Barrow is selected for this analysis covering one year period starting at 00:00:00 on 1 October, 2014. The other wind farms present in the cluster (Ormonde, Walney I, Walney II, and West of Duddon Sands) are modeled in the wake calculations.

Another set of AEP calculations is performed where the wind turbines from only Barrow are considered in wake calculations in order to investigate the impact of wake effects internal to Barrow. Each AEP result presented in this section indicates which turbines are modeled: either the whole cluster (270 WT) or only the turbines from Barrow (30 WT). For brevity, the Jensen and Gaussian wake models are referred in figures to as NOJ and GAU, respectively.

The cases only involving Barrow (30 WT) illustrate an idea of the energy loss from internal wakes. The cases with the entire cluster (270 WT) illustrate the losses from the combination of Barrow internal wakes and wakes from other wind farms acting on Barrow.

5.2.1 Time series based calculations

Figure 5.7 presents the time series based AEP results for Barrow in terms of percent change in predicted AEP relative to the AEP of a reference case. This reference case is chosen to be the AEP estimate based on the following parameters:

- H.point time series method
- Point wind climate from position of turbine BOW-B05
- Jensen wake model
- $k=0.04$
- Linear wake summation
- Only Barrow turbines modeled (30 WT)

This is justified by the fact that this combination is commonly used by others to simulate offshore wind farms (refer back to chapter 4). Note that the reference case is not necessarily the best at predicting real AEP. Turbine BOW-B05 is near the center of Barrow, and the corresponding reference case AEP value is 334044 [MWh].

The results for cases where only the turbines from Barrow (30 WT) are modeled are shown in Figure 5.7a, and results where all turbines are modeled (270 WT) are presented in Figure 5.7b. The value for the chosen reference case shows 0% change, as expected.

Note in Figure 5.7a that the differences between predictions from the H.point and G.all calculation methods for a particular wake model and model coefficient are small- on the order of 0.1% percent change with respect to the reference case AEP. Differences between H.all and G.all methods are even smaller. This suggests that the effect of including wind speed gradients when computing the AEP of Barrow is negligible when only Barrow is modeled.

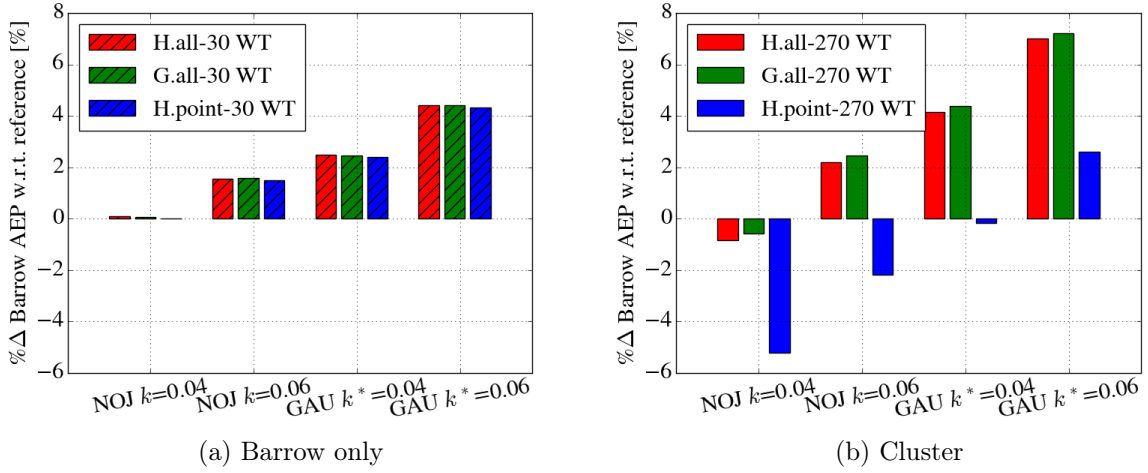


Figure 5.7: Percent change in AEP relative to the reference value for cases where (a) only Barrow is modeled and (b) the whole cluster is modeled with the time series based calculation methods

Figure 5.7 highlights that for cases with a given wake model and calculation method, the AEP increases for with increasing k or k^* . This makes sense due to the increased rate of wake expansion with downstream distance. The velocity deficit in the wakes recovers faster as a result. The AEP values predicted by the wake models using the same values for k and k^* differ by approximately 2% percent with respect to the reference AEP value. This implies some degree of sensitivity to the choice of the coefficients.

The inclusion of turbines from the other wind farms in the calculations impacts the AEP prediction of the methods in two main ways: through external wake effects on Barrow and through the definition of wind resource. H.all and G.all define the time step inflow conditions to representative flow cases based on the conditions at the positions of all modeled turbines. This has the effect of changing the wind resource when the other wind farms are modeled.

The H.point method wind resource stays the same regardless of the number of turbines modeled since it is based on the wind resource of a single point. The differences between the H.point (270 WT) and the reference case are therefore due exclusively to external wake effects. Figure 5.7b demonstrates this with decreases of predicted H.point AEP when the other wind farms are modeled.

From Figure 5.7, the H.point method appears to yield the most conservative results compared with the other calculation methods, but its results depend on how closely the point used for the wind resource definition captures the average wind climate of the area of interest.

Note from Figure 5.7b that the differences between results from the H.all and G.all calculation methods for a particular wake model and model coefficient are on the order of 0.25% different from the reference case AEP. This is still a small difference between the calculation methods, but more appreciable than in the cases where only Barrow is modeled (30 WT).

The time series based AEP predictions for Barrow indicate that influence of horizontal wind speed gradients over the area of Barrow is not felt strongly in the total AEP of Barrow. This may be explained by the fact that the wind direction sectors which show the most significant wind

speed gradients represent only a few percent of the simulated wind climate. Refer to the wind rose for turbine BOW - B05 in Figure 4.1a.

Even when horizontal wind speed gradients are present over the wind farm cluster area, the magnitude of these gradients over Barrow is small- see Figure 5.8a. Values presented are Sector 4, 75 [m] mean wind speeds normalized by the mean speed at the position of turbine BOW - B05 (highlighted in purple). Sector 4 is shown because the most significant mean gradients are present for that wind direction sector. 75 [m] corresponds to the hub height of the turbines in Barrow. It is clear from Figure 5.8 that the magnitudes of the mean gradients over the whole wind farm cluster are larger than those over just Barrow. This explains the slight increase in the difference between the H.all and G.all method predictions with the addition of the other wind farms (270 WT).

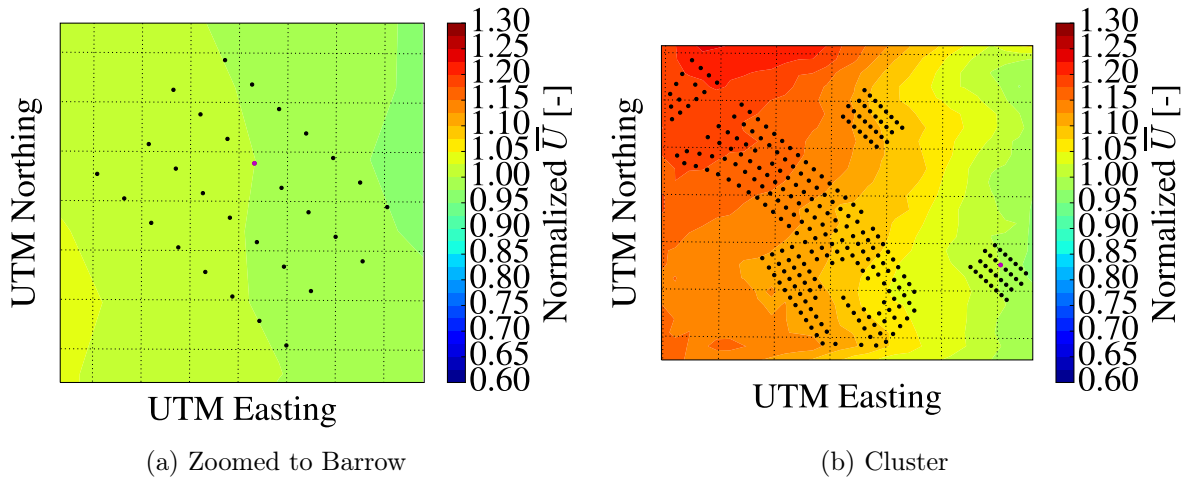
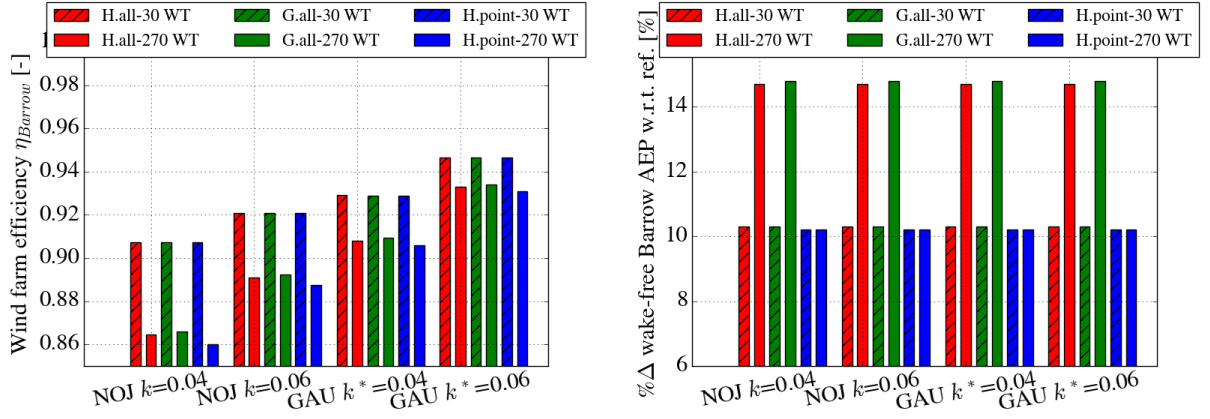


Figure 5.8: 75 [m] normalized mean wind speeds for Sector 4 across (a) Barrow and (b) zoomed out to the wind farm cluster. Values are normalized by the mean speed at turbine BOW - B05, shown in purple

To get a sense of how the addition of the other wind farms (270 WT) influences the wind resource, a wake-free reference AEP is computed in the manner described in subsection 4.6.1. This is not to be confused with the AEP prediction of the reference case. Wake-free reference AEP results are still presented in terms of percent change with this reference case.

Wind farm efficiency, η_{BOW} for the AEP results from different calculation methods and cases are presented in Figure 5.9a along with the corresponding wake-free reference AEP results in Figure 5.9b.

The impact of the inclusion of the other wind farms (270 WT) is observable in Figure 5.9a via the reduced wind farm efficiencies compared with 30 WT. Figure 5.9 emphasizes how the wind resource increases for the H.all and G.all methods with the addition of the other wind farms. This is due to the fact that the other turbines are further offshore, with higher mean wind speeds. The wake-free reference AEP does not change with the wake model since no wakes are involved. Figure 5.9 shows that the wind resource of the H.point method does not change, as expected. This explains why the H.point results show the largest η_{BOW} differences in Figure 5.9a.

(a) Wind farm efficiency η_{BOW} for different cases

(b) Wake free Barrow AEP for different cases

Figure 5.9: Time series based (a) Barrow wind farm efficiency η_{BOW} and (b) percent change between wake-free AEP values and the reference case AEP (time series based, NOJ, $k=0.04$, Barrow WT modeled)

For a particular method and wake model, the difference between η_{BOW} when only Barrow is modeled compared to when the entire cluster decreases with increasing k or k^* . Increasing the rate of wake expansion leads to reduced wake losses since the velocity deficit at the same downstream distance is reduced.

To analyze the impact of external wakes, results from the reference and H.point (270 WT) cases are presented in Table 5.1, along with the wind farm efficiency η_{BOW} . AEP differences are presented on the right of the table.

Case	H.point-30 WT	H.point-270 WT	AEP Difference
Barrow AEP (wake-free)	368165	368165	0
Barrow AEP (wakes)	334044	316596	17448
Difference	34121	51569	-17448
η_{BOW}	0.9073	0.8599	-

Table 5.1: Barrow H.point AEP [MWh] estimates with and without wake effects, modeling turbines from Barrow only and from the entire cluster

Taking the difference between wake-free reference and actual AEP when only Barrow is modeled (30 WT) yields 34121 [MWh]. This illustrates the effects of internal wake losses in Barrow with no upstream wind farms, and represents 10.2% of the reference AEP. The difference between wake-free reference and actual AEP when the whole cluster is modeled yields 51569 [MWh], or about 16.3% of the reference AEP, in line with the 10-20% range suggested by R. J. Barthelme, K. Hansen, et al. (2009). This illustrates the wake losses in Barrow due to internal and external wakes combined.

The difference in actual AEP with the addition of the other wind farms is 17448 [MWh], corresponding to 5.2% of the reference AEP when only Barrow is modeled. This gives indication of the impact of external wake effects on Barrow, although it should be noted that including

external wakes would change the impact of internal wakes by altering the wind speed at the first row of turbines in Barrow.

5.2.2 WAsP grid based calculations

Figure 5.10 presents the Barrow AEP results from WAsP grid based calculation methods terms of percent change relative to the same reference case as above (334044 [MWh] from time series based H.point, Jensen, $k=0.04$, 30 WT modeled). Keeping the same reference when computing percent change makes it easier to compare results from WAsP grid and time series based methods. AEP predictions with and without the presence of the other wind farms are analyzed to study the external wake effects.

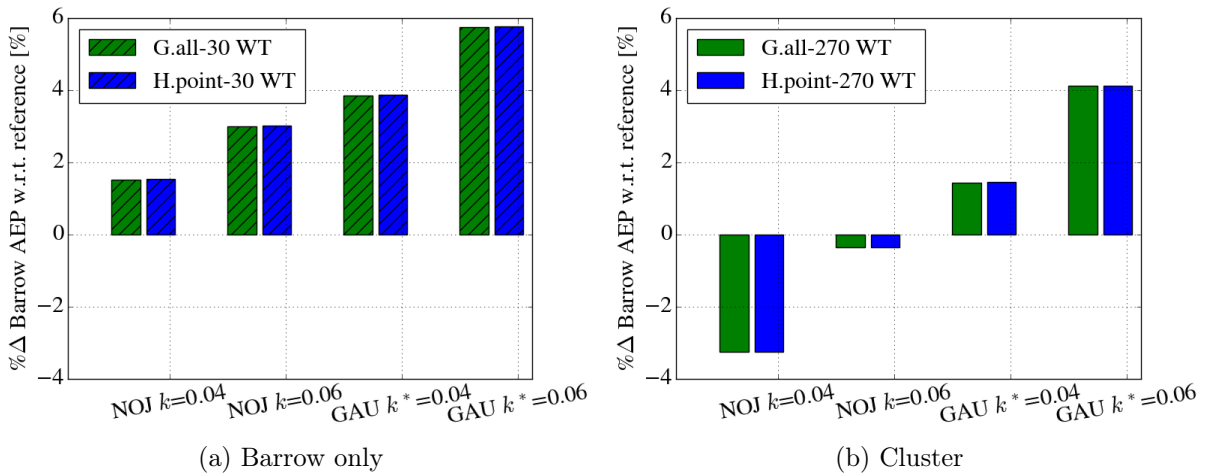


Figure 5.10: Percent change in WAsP grid Barrow AEP relative to reference case (time series based H.point, NOJ, $k=0.04$, 30 WT modeled) for (a) 30 WT and (b) 270 WT cases

Note that since the reference AEP case stays the same, all $\% \Delta$ values observed in Figure 5.10 are nonzero. Again, AEP predictions increase with k or k^* due to reduced wake losses. The results from the WAsP grid based methods indicate that the impact of wind speed gradients on the AEP of Barrow is small. Figure 5.10a shows that the differences between H.point and G.all Barrow AEP predictions are on the order of 0.1% for a given model and coefficient. This is also the case when all wind farms are considered in Figure 5.10b.

Note that wind resource grids do not change with the addition of the other wind farms. Therefore, differences in AEP with the addition of the other wind farms stem from the external wake effects on Barrow. This is explored via wind farm efficiency in Figure 5.11a.

Figure 5.11a indicates that the addition of the other wind farms reduces the wind farm efficiency for each case. Figure 5.11b underscores that the wind resource definition does not change with the addition of the other turbines. There is only a small difference in the wake-free reference AEP between the two WAsP grid methods. There is, however, a nearly 11.5% Δ in wake-free reference AEP between the WAsP grid methods and the reference time series based method. This needs further investigation to be able to effectively compare the WAsP grid AEP predictions with the time series based predictions.

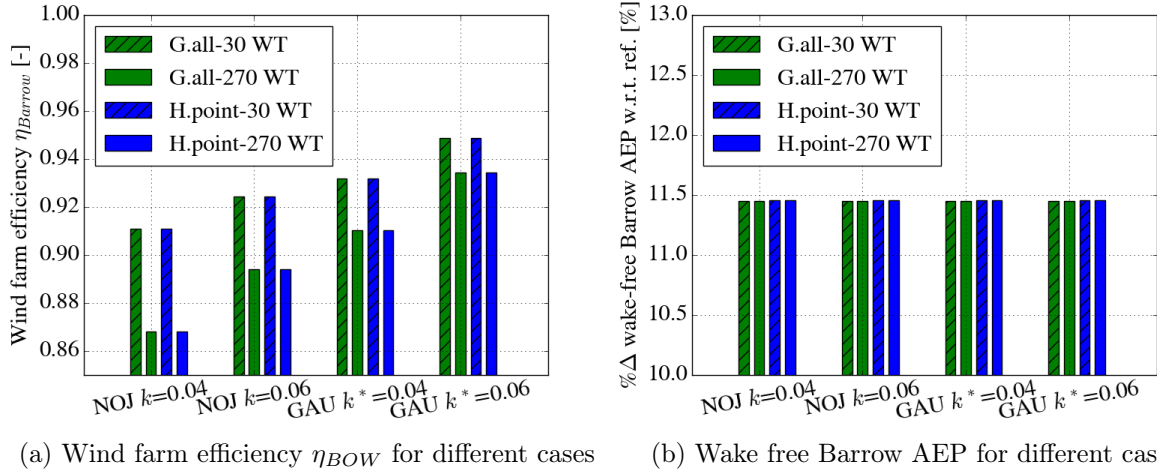


Figure 5.11: WASP grid based (a) Barrow wind farm efficiency η_{BOW} and (b) percent change between wake-free AEP values and the reference case AEP (time series based, NOJ, $k=0.04$, Barrow WT modeled)

Tables 5.2 and 5.3 illustrate the impact of wake effects for the H.point and G.all WASP grid method, respectively. The Jensen wake model with linear wake summation and $k=0.04$ are used.

Case	H.point-30 WT	H.point-270 WT	AEP Difference
Barrow AEP (wake-free)	372315	372315	0
Barrow AEP (wakes)	339184	323214	15970
Difference	33131	49101	-15970
η_{BOW}	0.9110	0.8681	-

Table 5.2: Barrow H.point WASP grid based AEP [MWh] results with and without wake effects, modeling Barrow only and the wind farm cluster

Case	G.all-30 WT	G.all-270 WT	AEP Difference
Barrow AEP (wake-free)	372284	372284	0
Barrow AEP (wakes)	339135	323179	15956
Difference	33149	49105	-15956
η_{BOW}	0.9110	0.8681	-

Table 5.3: Barrow G.all WASP grid based AEP [MWh] results with and without wake effects, modeling Barrow only and the wind farm cluster

As shown in Tables 5.2 and 5.3, the results from the G.all and H.all methods are nearly identical. The results from When only the turbines from Barrow are modeled, the wake losses correspond to 9.9% of the reference case AEP. This rises to 14.7% of reference case AEP when the whole wind cluster is modeled. This corroborates the results from the time series based approaches and indicates that external wake effects acting on Barrow are appreciable. This makes sense due

to the fact that the Walney and West of Duddon Sands wind farms are upstream from Barrow in the dominant wind directions.

5.2.3 Time series based sector-wise Barrow AEP

The results from the time series and WASP grid based calculation methods indicate small differences in homogeneous and gradient based AEP predictions for a particular model and coefficient. Since this small difference is attributed to the strength of wind speed gradients over barrow and the wind distribution, attention is turned to the sector-wise annual energy production to see if more significant differences between methods are noticeable for individual wind direction sectors.

A first approximation of this is obtained by filtering the results of the time series based approaches by the wind direction at turbine BOW - B05. The energy produced by the wind farm at each time step is therefore associated with the wind direction sector occurring at BOW - B05, enabling a calculation of each sector's annual energy production. This choice to filter at one point ignores wind direction gradients, which is assumed to be acceptable over the area of Barrow.

The resulting sector-wise Barrow AEP values are presented for cases where only Barrow is modeled and cases where all turbines are modeled in Figure 5.12 and Figure 5.13, respectively. Values are in terms of percent change relative to each sector's respective production from the reference case (time series based H.point method with $k=0.04$, linear wake summation, 30 WT modeled). The two figures have the same vertical axis limits to facilitate comparison.

As expected in Figure 5.12, the reference case shows 0% change with itself in each sector. Sectors 1-3 show the largest percent changes between the reference (H.point) method and the other two methods, with a maximum in Sector 2 of about 1.7%. However the largest difference between the H.all and G.all methods, found in Sector 1, is less than 0.5% with respect to the reference case.

Figure 5.13 paints a different picture when the other turbines are considered.

As observed in Figure 5.13, percent changes relative to the reference case are as high as 40% for the H.all and G.all methods. This is due to the fact that the wind resource definition for those methods changes with the introduction of more turbines into the calculation. For the H.point method the wind resource does not change with the addition of the other wind farms since the single point climate is taken near the center of Barrow. This explains why the percent change values of the H.all and G.all methods are so high in Figure 5.13.

To separate out the effect of the changing wind resource definition with the addition of the other wind farms, the differences between AEP results from the H.all and G.all methods are considered since the wind resource changes for both methods. Figure 5.13 indicates an increase in the difference between the H.all and G.all results for Sectors 1-5 with the consideration of the other wind farms. For Sector 2 this difference is nearly 5% change with respect to the reference. It is less than 0.5% when only the turbines from Barrow are modeled. The gradients observed for wind direction Sectors 1-5 in Figure 4.2 are more significant over the area of the wind farm cluster than over the area of Barrow. The increased difference between the H.all and G.all methods when modeling all turbines indicates that using a gradient based analysis may be appropriate when considering winds from gradient prone sectors over a large area. To investigate this, the AEP of the entire cluster is analyzed in section 5.3.

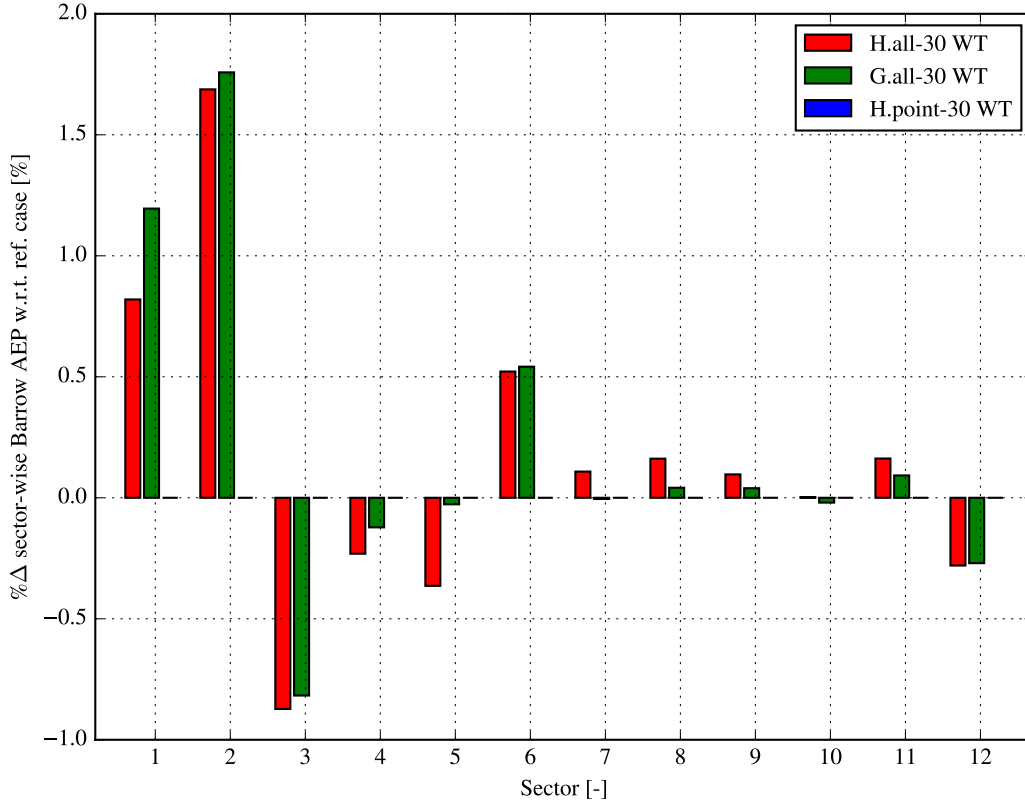


Figure 5.12: Sector-wise percent change in Barrow AEP relative to reference case. Only turbines from Barrow are modeled (30 WT)

In Figure 5.13 Sectors 9-12 show differences in the H.point AEP values. The magnitudes of the H.point sector-wise AEP values should be similar with and without the addition of the other wind farms, since the H.point wind climate does not change. The difference should therefore be due to wake interaction from other wind farms. This is highlighted more clearly in Figure 5.14 where absolute magnitudes of H.point AEP in [GWh] are presented as well as the bin frequency based on the filtering method described above.

The decrease in H.point AEP with the addition of the other wind farms in Figure 5.15 highlights the presence of external wakes acting on Barrow for Sectors 9-12. As expected, the sectors with the highest number of occurrences at BOW-B05 over the course of the year produce the most energy. Sectors 1-6 are less frequent and contribute less to the overall AEP. According to Figure 4.2, these are the sectors for which the mean wind speed gradients are most prominent over the wind farm cluster area.

5.2.4 Barrow wind farm efficiency

In this section the directional efficiency of Barrow is explored. The definition directional wind farm efficiency utilized here is the same as Equation 4.2 applied for a specific wind direction.

This was done in five stages, with each stage representing the addition of a wind farm to the model. Thus, the first stage offers an indication of the efficiency of Barrow alone due to internal

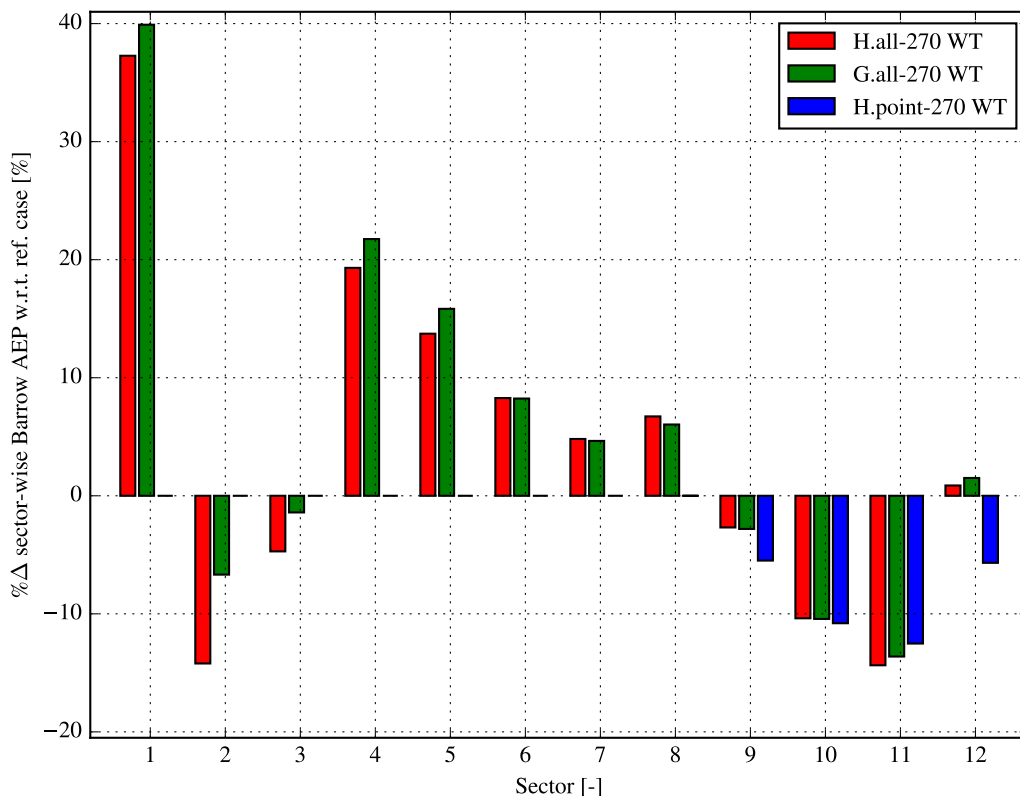


Figure 5.13: Sector-wise percent change in Barrow AEP relative to reference case. Turbines from the entire cluster are modeled (270 WT)

wake effects. Stage five represents the directional efficiency of Barrow due to internal wake effects and wake effects from all of the other wind farms. The wind farms are added in order of increasing distance from Barrow (top down in legend).

Results utilizing the Jensen wake model with $k=0.04$ and quadratic wake summation are presented in steps of 1° for a wind speed of 8 [m/s] are visible in Figure 5.15. The color of the line represents Barrow's efficiency modeling the wind farm of that color, plus all the previous stages. A map of the wind farm cluster is shown in the center for reference.

Note the lowest efficiencies when the wind direction aligns with the rows of turbines in Barrow. The troughs do not narrow to a single point since the Jensen model assumes a tophat profile with a starting diameter corresponding to the turbine rotor diameter.

The majority of the wake losses from additional wind farms occur with the addition of West of Duddon Sands, visible as the difference between light blue and green lines. This makes sense due to the fact that the wind rose is dominated by wind directions from the west and southwest. The effect of Walney II is minimal, visible as the difference from pink to dark blue. This makes sense because Walney II is furthest from Barrow.

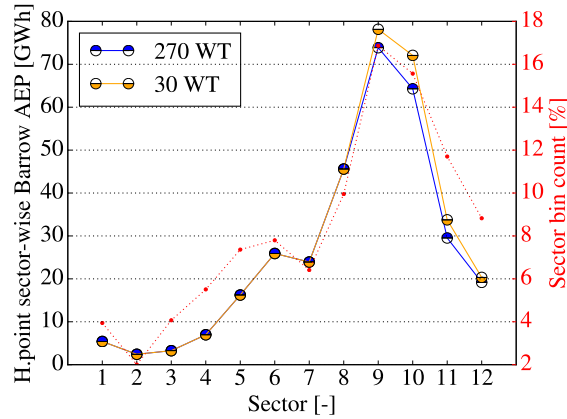


Figure 5.14: Sector-wise Barrow AEP results in [GWh] from time series based H.point methods with $k=0.04$, linear wake summation. 30 WT indicates only Barrow was modeled and 270 WT indicates that the turbines from the entire cluster are included. Wind direction sector bin count based on the filtering wind direction at BOW-B05 indicated in red

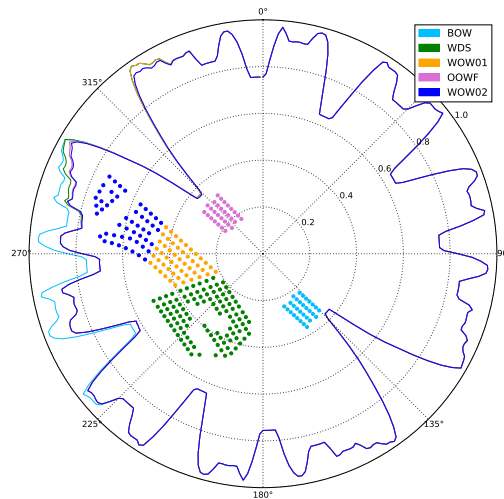


Figure 5.15: Barrow wind farm efficiency by direction - in stages

5.3 Cluster AEP

The AEP of the entire wind farm cluster is computed with the five different methods to investigate the impact of accounting for horizontal wind speed gradients over a larger area. Again results are presented in terms of percent change with the AEP of a reference case defined by:

- H.point time series method
- Point wind climate from position of turbine BOW-B05
- Jensen wake model
- $k=0.04$

- Linear wake summation

The corresponding AEP value for the cluster in the reference case is 3870 [GWh].

5.3.1 Time series based calculations

AEP results and cluster efficiency $\eta_{cluster}$ from time series based method are presented in Figure 5.16a and Figure 5.16b, respectively.

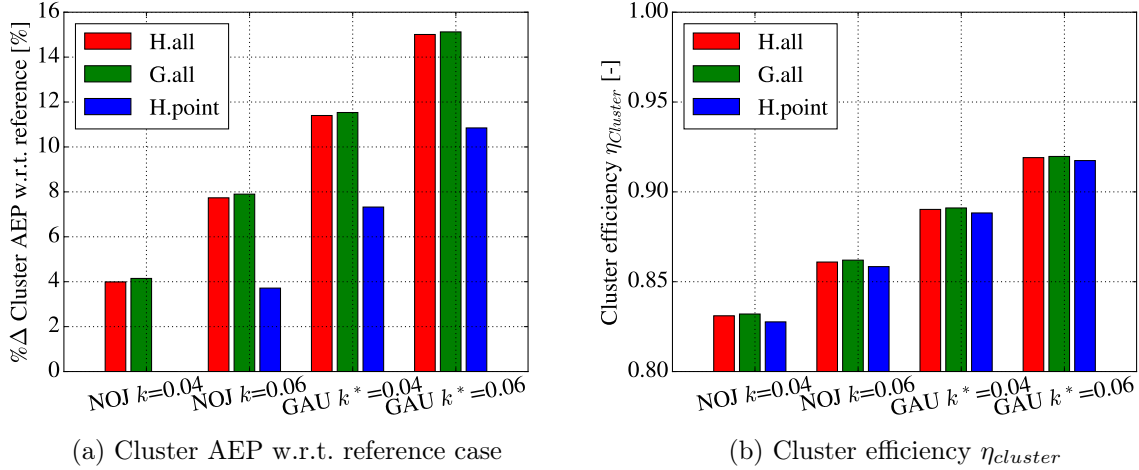


Figure 5.16: Time series based (a) percent change between AEP values and the reference case AEP and (b) cluster efficiency $\eta_{cluster}$

Figure 5.16a indicates the reference case shows 0% change with itself, as expected. The H.point method shows differences compared with the other methods of about 4% due to the fact that the H.point reference position is taken near the center of Barrow. The single point wind climate taken near the center of Barrow does not represent the average wind climate over the cluster as well as it represents the average climate of Barrow. This is highlighted in Figure 4.2.

Smaller differences between H.all and G.all methods are observable in both the AEP values and the efficiencies presented in Figure 5.16b. This difference is on the order of 0.1% a given wake model and coefficient. This indicates that including gradients in the calculation of the AEP of the Irish Sea cluster does not have a large impact on the result. This is the same trend as seen in the investigations of Barrow and is attributed to the prominence of over sea wind direction sectors for which wind speed gradients have lower magnitudes.

A year long time series of the difference between the predicted H.all $P_{tot,j}$ and and G.all $P_{tot,j}$ is presented in Figure 5.17. This was computed for the cluster based on the Jensen wake model with $k=0.04$ and linear wake summation. Figure 5.17 reveals that the small difference the methods predict in total cluster AEP is due to positive and negative differences in predicted power canceling over the course of the year. The greatest and least time step power differences between the methods were identified to be the result of situations where \bar{U} was just under and just above the cut-out wind speed $U_{cut-out}$. This makes sense due to the fact that the H.all may unnecessarily predict the shut off numerous turbines when $\bar{U} > U_{cut-out}$.

This highlights one of the main challenges when investigating AEP: that errors or differences may cancel in the long run.

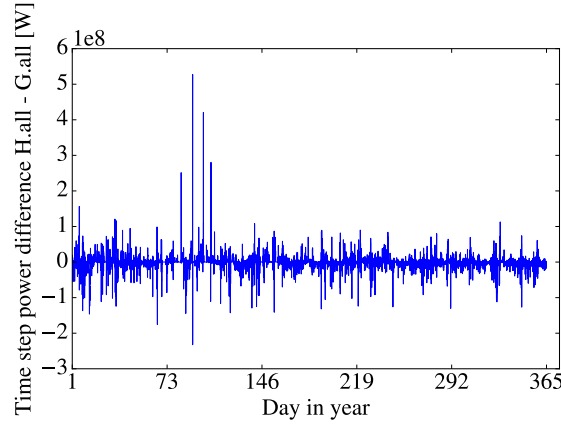


Figure 5.17: Year long time series of power difference predicted by the H.all and G.all time series methods. Day 1 corresponds to 1 October, 2014

5.3.2 WAsP grid based calculations

To investigate the choice of the H.point wind climate, AEP results from the WAsP grid based method are presented in Figure 5.18. In Figure 5.18a the H.point calculation is computed twice. Once based on the wind climate at turbine BOW-B05, and once based on the wind climate from the position of turbine WOW01-F1. Results are presented in terms of percent change compared to the reference cluster AEP. Figure 5.18b shows the cluster efficiency.

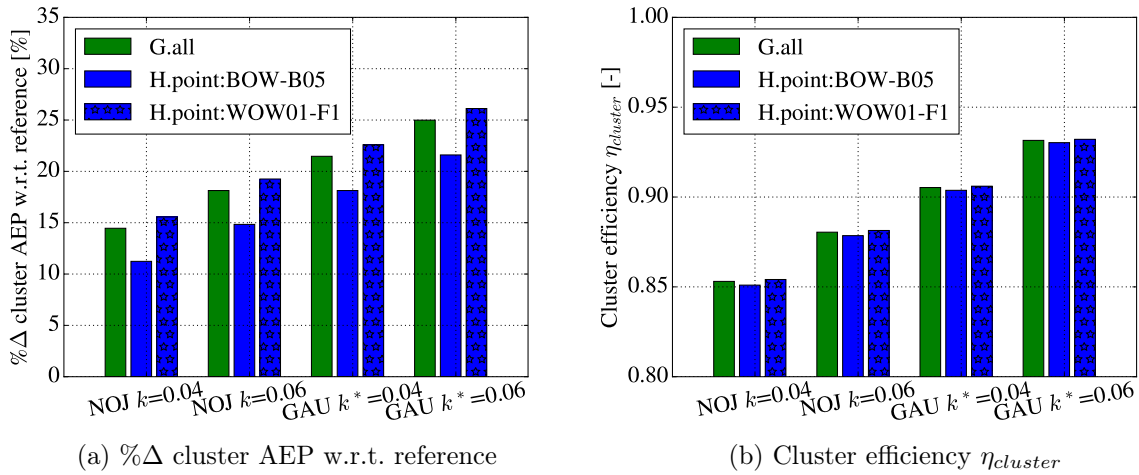


Figure 5.18: WAsP grid based cluster (a) AEP results and (b) cluster efficiency

By comparing the predictions of the two H.point calculations in Figure 5.18a, one observes that changing the wind climate of the H.point method to the position of turbine WOW01 - F1 (near the center of the cluster) yields a smaller percent difference between G.all and H.point results (approximately a difference of 0.75% instead of 3% change with respect to the reference). This appears to be a better choice, and the result from this change is in line with the findings of Alfredo Peña, K. S. Hansen, et al. (2017) which found less than 1% AEP difference between homogeneous and gradient based calculation methods.

5.3.3 Time series based sector-wise cluster AEP

The time series based AEP is broken down by sector in Figure 5.19 in the same manner as above for Barrow. The H.point wind climate is taken at the position of turbine BOW-B05 in this case and the sectors are filtered based on the wind direction time series at that position.

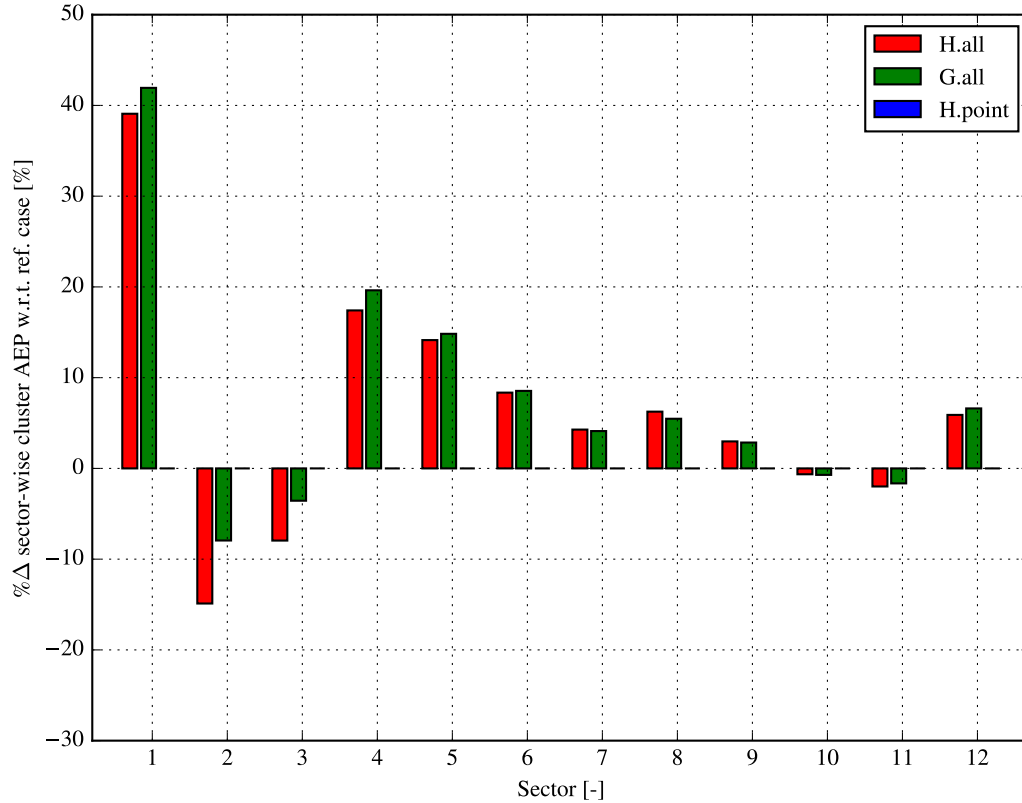


Figure 5.19: Sector-wise cluster AEP results for different methods presented as percent change relative to the reference case (time series based H.point with $k=0.04$). Filtered based on the wind direction time series at BOW-B05

The percent change between H.point and the other methods shows large differences in most sectors. By defining the wind resource for the whole cluster to match a point at the center of barrow, the gradients observed over the cluster in Sectors 1-6 are ignored. Refer to Figure 4.2.

More appreciable differences are noticeable between the H.all and G.all approaches for sectors 1-4 represent overland wind directions.

The WASP grid based results suggest that performing the cluster AEP H.point calculation based on the climate at WOW01-F1, would better represent the average wind climate over the area of the cluster.

5.4 Uncertainty

Using Equation 4.44, the uncertainty is calculated as a percentage of the AEP. Based on the reference case for the cluster (38670 [GWh]), this corresponds to 3.12% of AEP, meaning that

differences between methods smaller than this level are within the bounds of the wake model uncertainty. For these situations, results cannot be said to be different with confidence. The wake models were implemented in the same way for both cases, although the inflow was defined differently according to the calculation methods.

The absolute differences between the G.all and H.all methods exceeded this threshold using the Jensen wake model with $k=0.04$ for the time series based methods in wind direction sectors 2 and 3 (absolute differences of 6.94% and 4.39% of the reference case AEP, respectively). For these sectors the wind comes from over the land and horizontal wind speed gradients due to the coast are expected.

The differences observed with the WAsP grid methods compared to this reference case were also found to be substantial.

Chapter 6

Conclusions and Future Work

This thesis investigates the impact of horizontal wind speed gradients on AEP estimation for an offshore wind farm cluster in the Irish Sea by comparing AEP results from five calculation methods. Two of the methods account for wind speed gradients over a site, while the remaining three methods assume inflow homogeneity.

Flow cases for a simple two turbine wind farm are used to explore the differences in the time series based calculation methods. The two turbine wind farm is too simplified to draw conclusions about wind speed gradients in a cluster of wind farms, but predicted power results from a nonaligned wind direction suggest that the a homogeneous method (H.all) yields errors compared with the true power when the turbines have a free stream wind speed difference. The gradient method (G.all), on the other hand, is able to predict the true wind farm power in this scenario. This difference between the H.all and G.all methods is due to the fact that the cube of the mean of some numbers U_1 , U_2 , and U_i is not always the same as the mean of the cubes of those numbers. The prediction of the H.point method was found to depend highly on the selected reference point.

When analyzing just one wind farm- Barrow- differences in AEP values predicted by the time series based G.all and H.all methods were found to be small- between 0.1%-0.25% of a reference case AEP. Similar results were observed when comparing the G.all and H.point WAsP grid based methods to one another. These results indicate that for this wind farm, the effect of modeling gradients in the above manner is small. This is attributed to the low magnitude of wind speed variation over Barrow.

Differences between the G.all and H.all time series based methods when examining the entire wind farm cluster AEP were also found to be on the order of 0.1%, and up to 0.75% of the reference case AEP for the WAsP grid based methods. This suggests that the overall impact of accounting for wind speed gradients in AEP calculations is small even over a large area of the Irish Sea. A Only after filtering results by wind direction sector, were differences between the G.all and H.all time series methods larger than the assumed wake model uncertainty, and only for wind direction Sectors 2 and 3 (inflow from land). Their overall contribution to the total AEP is limited by the fact that these wind directions represent a small percentage of the wind rose, and have lower mean wind speeds than the other direction sectors. Additionally, positive and negative differences between the H.all and G.all time series methods were found to balance over the year.

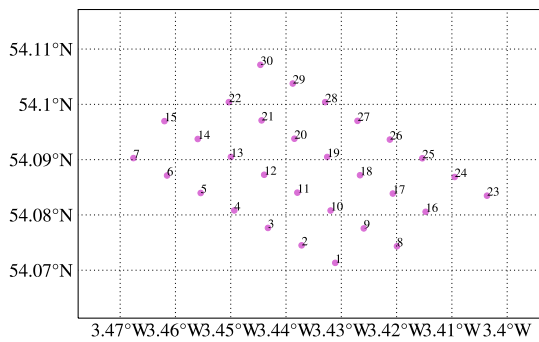
At this point it cannot be said if the gradient based analyses implemented in this thesis offers an improvement over the methods which assume homogeneous flow. Future work could consist of quantifying the magnitude of gradient necessary for these methods to lead to significant differences in the H.all and G.all time series methods. Additional investigation is needed into the conditions under which these methods yield different predictions. This could include investigating the impact of atmospheric stability both this and fetch influence wind speed gradients in the coastal zone.

Appendices

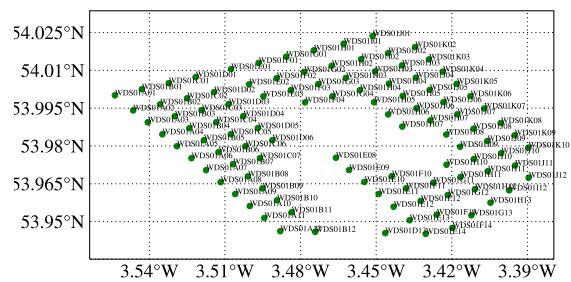
Appendix A

Wind farm maps

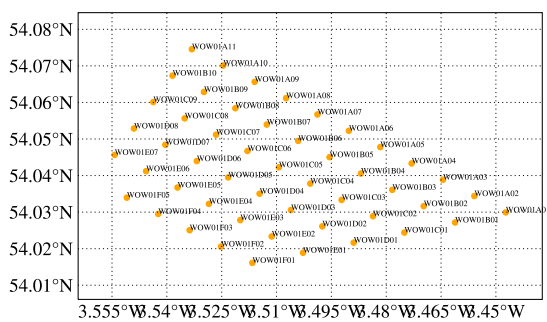
The maps of the wind farms considered in the analysis are included for reference. This excludes the map of Barrow, which was presented in the text.



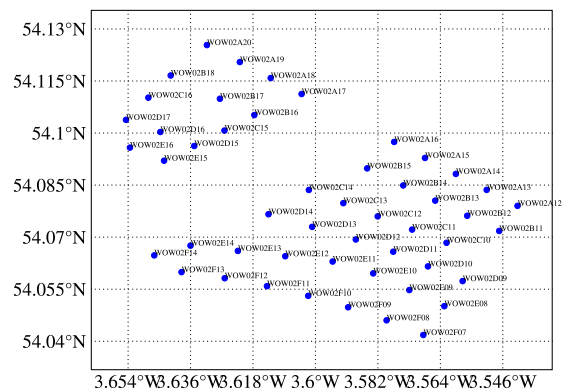
(a) OOWF



(b) WDS



(c) WOW01



(d) WOW02

Figure A.1: Wind farm maps

Appendix B

WRF wind climate maps - Additional heights

Sector	Direction Range [°]	$U_{norm,75}$ [m/s]	$U_{norm,83.5}$ [m/s]	$U_{norm,90}$ [m/s]
1	$0 \pm 15^\circ$	6.02	6.00	5.98
2	$30 \pm 15^\circ$	4.98	5.02	5.03
3	$60 \pm 15^\circ$	4.98	5.00	5.02
4	$90 \pm 15^\circ$	5.76	5.79	5.82
5	$120 \pm 15^\circ$	7.86	7.90	7.94
6	$150 \pm 15^\circ$	9.15	9.21	9.25
7	$180 \pm 15^\circ$	9.35	9.40	9.41
8	$210 \pm 15^\circ$	10.89	10.99	11.08
9	$240 \pm 15^\circ$	11.38	11.52	11.60
10	$270 \pm 15^\circ$	11.12	11.20	11.25
11	$300 \pm 15^\circ$	9.02	9.06	9.09
12	$330 \pm 15^\circ$	7.73	7.76	7.78

Table B.1: \bar{U} [m/s] at turbine BOW-A07 for different direction sectors and heights

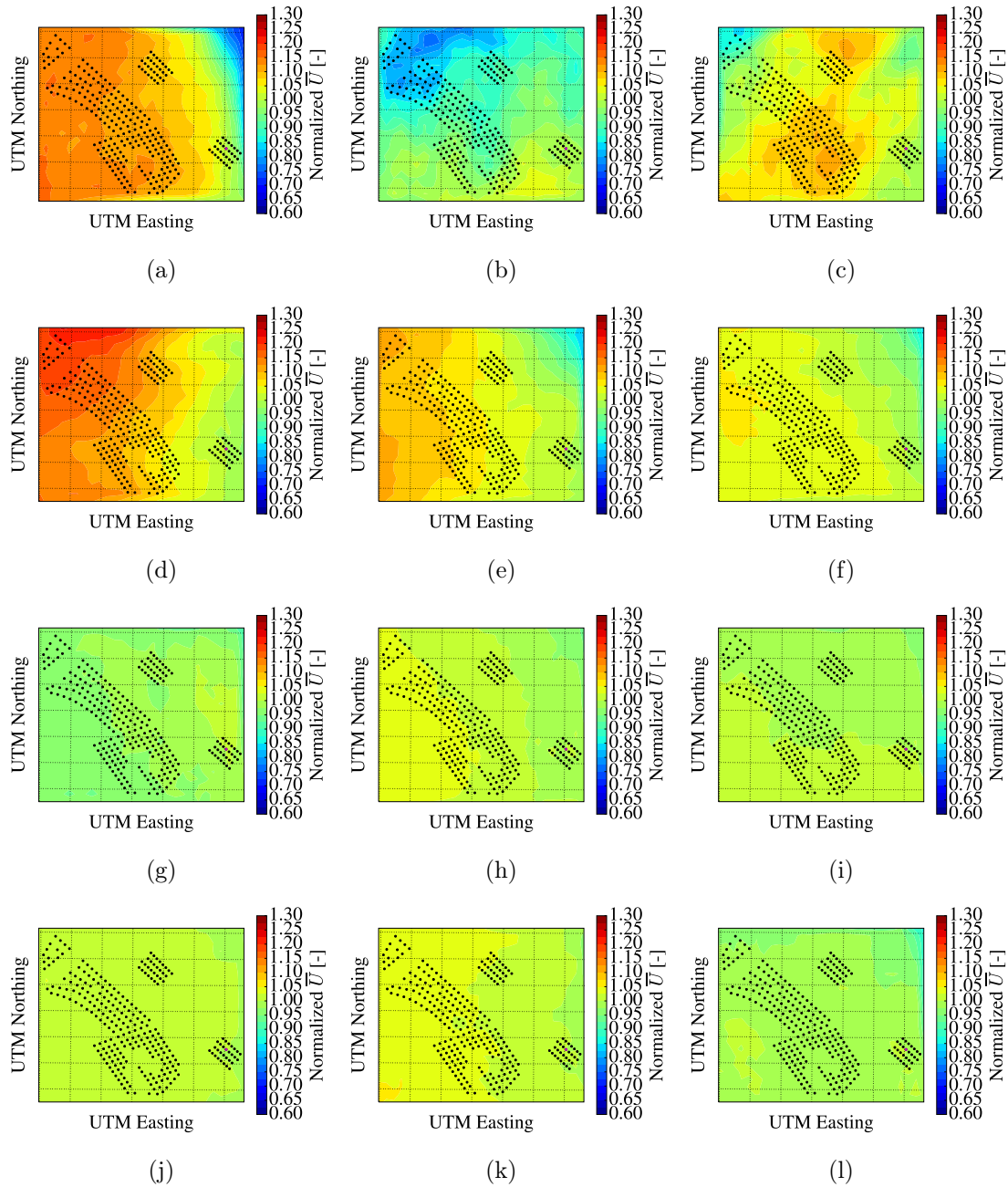


Figure B.1: Normalized WRF \bar{U} per sector at 83.5 [m]

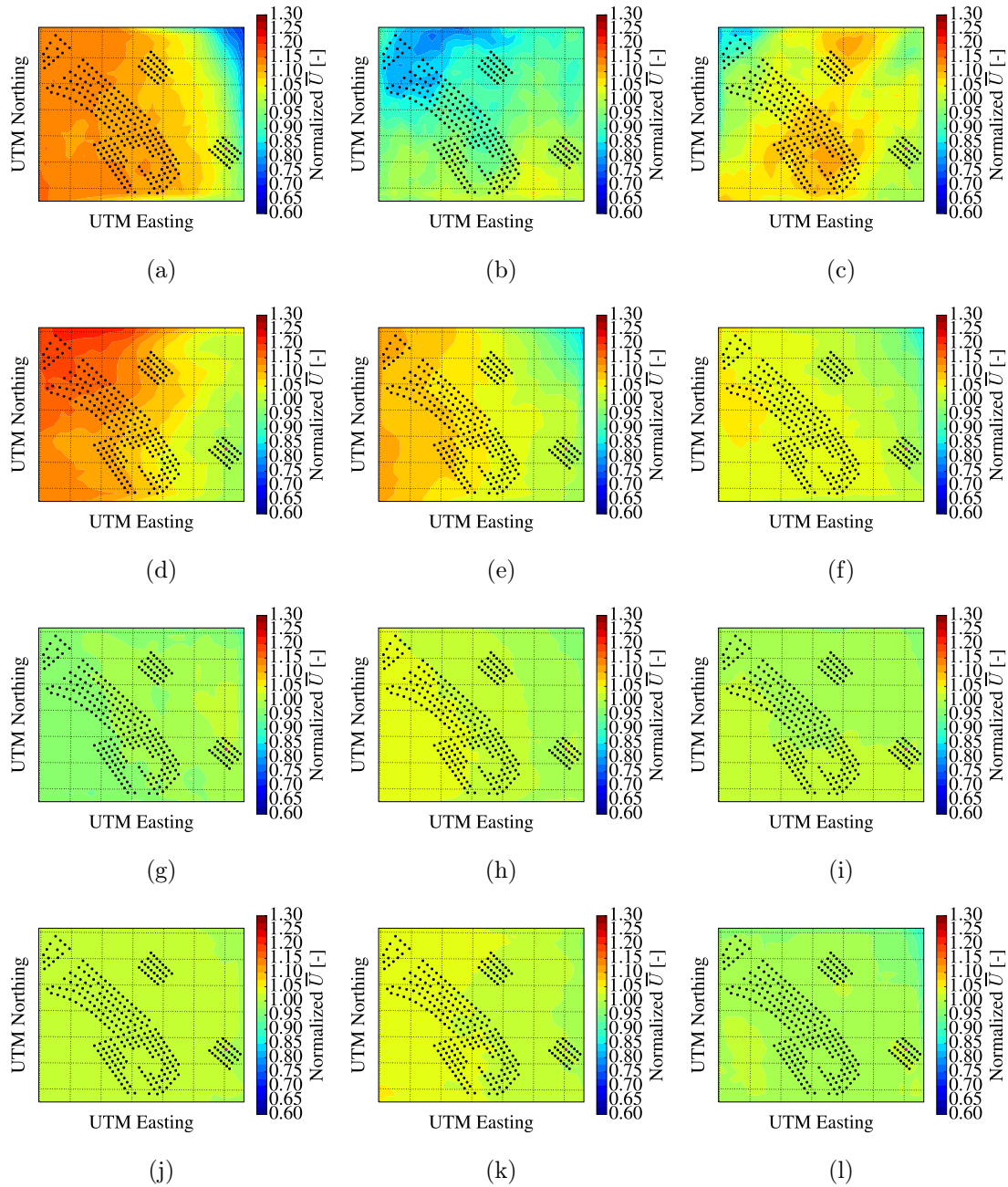


Figure B.2: Normalized WRF \bar{U} per sector at 90 [m]

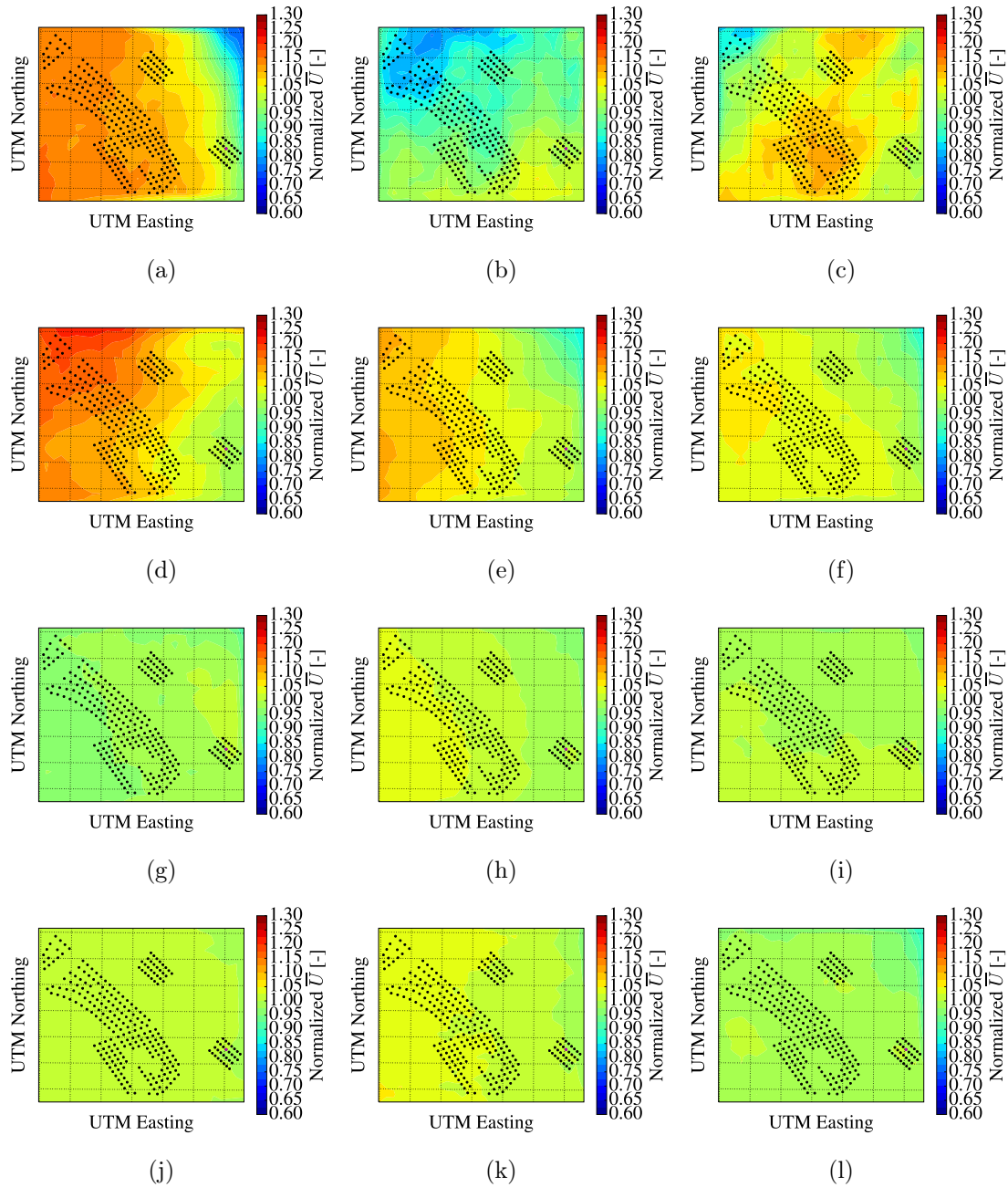


Figure B.3: Normalized WRF \bar{U} per sector at 100 [m]

Bibliography

- Jensen, N. O. (1983). “A note on wind generator interaction.” In: *Riso National Laboratory Roskilde* 2411, pp. 1–16. ISSN: 01676105. DOI: Riso-M-2411.
- Katić, I., J. Højstrup, and N. O. Jensen (1987). “A Simple Model for Cluster Efficiency.” In: *EWEC’86*. Ed. by W. Palz and E. Sesto. Vol. 1. Rome: European Wind Energy Association Conference and Exhibition.
- Sanderhoff, Peter (1993). *PARK - User’s Guide. A PC-program for calculation of wind turbine park performance*. Roskilde, Denmark.
- Pryor, S. C. and R. J. Barthelmie (1998). *Analysis of the effect of the coastal discontinuity on near-surface flow*. Tech. rep. 7, pp. 882–888. URL: <https://hal.archives-ouvertes.fr/hal-00316418>.
- DWEA (2003). *Power Curve of a Wind Turbine*. Web. URL: <http://xn--drmstrre-64ad.dk/wp-content/wind/miller/windpower%5C%20web/en/tour/wres/pwr.htm>.
- Vermeer, L. J., J. N. Sørensen, and A. Crespo (2003). “Wind turbine wake aerodynamics.” In: *Progress in Aerospace Sciences* 39.6-7, pp. 467–510. ISSN: 03760421. DOI: 10.1016/S0376-0421(03)00078-2.
- Christiansen, Merete Bruun and C. B. Hasager (2005). “Wake effects of large offshore wind farms identified from satellite SAR.” In: *Remote Sensing of Environment* 98.2-3, pp. 251–268. ISSN: 00344257. DOI: 10.1016/j.rse.2005.07.009.
- Barthelmie, R. J., S. T. Frandsen, et al. (2007). “Modelling and measurements of power losses and turbulence intensity in wind turbine wakes at middelgrunden offshore wind farm.” In: *Wind Energy* 10.6, pp. 517–528. ISSN: 10954244. DOI: 10.1002/we.238.
- Barthelmie, R.J. et al. (2007). “Offshore Coastal Wind Speed Gradients: Issues for the Design and Development of Large Offshore Windfarms.” In: *Wind Engineering* 31.6, pp. 369–382. ISSN: 0309-524X. DOI: 10.1260/030952407784079762. URL: <http://journals.sagepub.com/doi/10.1260/030952407784079762>.
- Renkema, Douwe J (2007). “Validation of wind turbine wake models using wind farm data and wind tunnel measurements.” In: pp. 1–115. ISSN: 0309-524X. DOI: 10.1260/030952408786411912. URL: <http://lr.home.tudelft.nl/fileadmin/Faculteit/LR/Organisatie/Afdelingen%7B%5C%7Den%7B%5C%7DLeerstoelen/Afdeling%7B%5C%7DAEWE/Wind%7B%5C%7DEnergy/Education/Masters%7B%5C%7DProjects/Finished%7B%5C%7DMaster%7B%5C%7Dprojects/doc/Douwe%7B%5C%7DRenkema%7B%5C%7Dr.pdf>.
- Barthelmie, R. J., K. Hansen, et al. (2009). “Modelling and measuring flow and wind turbine wakes in large wind farms offshore.” In: *Wind Energy* 12.5, pp. 431–444. ISSN: 10954244. DOI: 10.1002/we.348.

- Burton, Tony (Powys) et al. (2009). *Wind Energy Handbook*. Second Edition. Chichester: John Wiley & Sons Ltd. ISBN: 9780072483116. DOI: 10.1037/023990.
- Manwell, J.F. (University of Massachusetts), J.G. (University of Massachusetts) McGowan, and A.L. (DNV) Rogers (2009). *Wind Energy Explained - Theory, Design, and Application*. Second Edi. John Wiley & Sons Ltd. ISBN: 9780470015001.
- Barthelmie, R. J., S. C. Pryor, et al. (2010). “Quantifying the impact of wind turbine wakes on power output at offshore wind farms.” In: *Journal of Atmospheric and Oceanic Technology* 27.8, pp. 1302–1317. ISSN: 07390572. DOI: 10.1175/2010JTECHA1398.1.
- Barthelmie, R.J. and L. E. Jensen (2010). “Evaluation of wind farm efficiency and wind turbine wakes at the Nysted offshore wind farm.” In: *Wind Energy*. ISSN: 11283602. DOI: 10.1002/we. arXiv: arXiv:1006.4405v1.
- Gaumond, M., P.E. Réthoré, et al. (2012). “Benchmarking of Wind Turbine Wake Models in Large Offshore Windfarms.” In: *The Science of Making Torque from the Wind Conference*. Vol. 1. Oldenburg, Germany.
- Barthelmie, R. J., K. S. Hansen, and S. C. Pryor (2013). “Meteorological controls on wind turbine wakes.” In: *Proceedings of the IEEE* 101.4, pp. 1010–1019. ISSN: 00189219. DOI: 10.1109/JPROC.2012.2204029.
- Gaumond, M., P-E ; Réthoré, et al. (2013). “Evaluation of the wind direction uncertainty and its impact on wake modeling at the Horns Rev offshore wind farm.” In: *WIND ENERGY*. DOI: 10.1002/we.1625. URL: http://orbit.dtu.dk/files/56375879/Evaluation%7B%5C_%7Dof%7B%5C_%7Dthe%7B%5C_%7Dwind%7B%5C_%7Ddirection.pdf.
- Bastankhah, Majid and Fernando Porté-Agel (2014). “A new analytical model for wind-turbine wakes.” In: *Renewable Energy* 70, pp. 116–123. ISSN: 09601481. DOI: 10.1016/j.renene.2014.01.002. URL: <http://dx.doi.org/10.1016/j.renene.2014.01.002>.
- Wind measurement campaigns offshore and how do they create value* (2014). Dong Energy Windpower. Wind Power Monthly Wind resource Assessment Conference.
- Moriarty, Patrick et al. (2014). “IEA-task 31 WAKEBENCH: Towards a protocol for wind farm flow model evaluation. Part 2: Wind farm wake models.” In: *Journal of Physics: Conference Series* 524.1. ISSN: 17426596. DOI: 10.1088/1742-6596/524/1/012185.
- Nygaard, Nicolai Gayle (2014). “Wakes in very large wind farms and the effect of neighbouring wind farms.” In: *Journal of Physics: Conference Series* 524.1. ISSN: 17426596. DOI: 10.1088/1742-6596/524/1/012162.
- Peña, Alfredo, Pierre Réthoré, and Ole Rathmann (2014). “Modeling large offshore wind farms under different atmospheric stability regimes with the Park wake model.” In: *Renewable Energy* 70, pp. 164–171. ISSN: 09601481. DOI: 10.1016/j.renene.2014.02.019. URL: <http://dx.doi.org/10.1016/j.renene.2014.02.019>.
- Wang, H. et al. (2014). “Profiles of wind and turbulence in the coastal atmospheric boundary layer of Lake Erie.” In: *Journal of Physics: Conference Series* 524.1. ISSN: 17426596. DOI: 10.1088/1742-6596/524/1/012117.
- Badger, J. et al. (2015). “Comparing satellite SAR and wind farm wake models.” In: *Journal of Physics: Conference Series* 625, p. 012035. ISSN: 1742-6588. DOI: 10.1088/1742-6596/625/1/012035.

- Barthelmie, R.J., M.J. Churchfield, et al. (2015). “The role of atmospheric stability / turbulence on wakes at the Egmond aan Zee offshore wind farm.” In: *Journal of Physics: Conference Series*. DOI: 10.1088/1742-6596/625/1/012002.
- Feng, Ju and Wen Zhong Shen (2015). “Modelling wind for wind farm layout optimization using joint distribution of wind speed and wind direction.” In: *Energies* 8.4, pp. 3075–3092. DOI: 10.3390/en8043075.
- Hansen, K. S. et al. (2015). “Simulation of wake effects between two wind farms.” In: *Journal of Physics: Conference Series* 625.1. ISSN: 17426596. DOI: 10.1088/1742-6596/625/1/012008.
- Hasager, Charlotte B. et al. (2015). “Wind climate estimation using WRF model output: method and model sensitivities over the sea.” In: *International Journal of Climatology* 35.12, pp. 3422–3439. DOI: 10.1002/joc.4217.
- Laan, M. P. van der et al. (2015). “The k-epsilon-fP model applied to wind farms M.” In: *Wind Energy* 18, pp. 2065–2084. DOI: 10.100/we.1804.
- Nygaard, Nicolai Gayle (2015). “Systematic quantification of wake model uncertainty.” In: *EWEA Offshore 2015*, pp. 1–10.
- Van Der Laan, M. P. et al. (2015). “Predicting wind farm wake interaction with RANS: An investigation of the Coriolis force.” In: *Journal of Physics: Conference Series* 625.1. ISSN: 17426596. DOI: 10.1088/1742-6596/625/1/012026.
- Volker, P.J.H. et al. (2015). “The explicit wake parametrisation V1.0: A wind farm parametrisation in the mesoscale model WRF.” In: *Geoscientific Model Development* 8.11, pp. 3715–3731. ISSN: 19919603. DOI: 10.5194/gmd-8-3715-2015.
- Göçmen, Tuhfe et al. (2016). “Wind turbine wake models developed at the technical university of Denmark: A review.” In: *Renewable and Sustainable Energy Reviews* 60, pp. 752–769. ISSN: 18790690. DOI: 10.1016/j.rser.2016.01.113. URL: <http://dx.doi.org/10.1016/j.rser.2016.01.113>.
- Nygaard, Nicolai Gayle and Sidse Damgaard Hansen (2016). “Wake effects between two neighbouring wind farms.” In: *Journal of Physics: Conference Series* 753.3. ISSN: 17426596. DOI: 10.1088/1742-6596/753/3/032020.
- Sørensen, Jens N. and Carlos Ferreira (2016). “Aerodynamics.” In: *Long Term Challenges in Wind Energy - A Research Agenda by the European Academy of Wind Energy*. Ed. by G. van Kuik and Joachim Peinke. 6th. Springer International Publishing, Switzerland. Chap. Chapter 3, pp. 17–26. ISBN: 9783319469188. DOI: 10.1007/978-3-319-46919-5.
- van der Laan, M. P. and N. N. Sørensen (2016). “Why the Coriolis force turns a wind farm wake to the right in the Northern Hemisphere.” In: *Journal of Physics: Conference Series* 753.3, pp. 285–294. ISSN: 17426596. DOI: 10.1088/1742-6596/753/3/032031.
- Walker, Keith et al. (2016). “An evaluation of the predictive accuracy of wake effects models for offshore wind farms.” In: *Wind Energy* 19, pp. 979–996. ISSN: 11283602. DOI: 10.1002/we. arXiv: arXiv:1006.4405v1.
- BNEF (2017). *Global Offshore Wind Market Set to Grow Sixfold by 2030*. Web. URL: <https://about.bnef.com/blog/global-offshore-wind-market-set-to-grow-sixfold-by-2030/>.
- Pablo Murcia, Juan (2017). “Uncertainty Quantification in Wind Farm Flow Models.” PhD thesis. Technical University of Denmark.

- Peña, Alfredo, K. S. Hansen, et al. (2017). “On wake modeling, wind-farm gradients and AEP predictions at the Anholt wind farm.” In: *Wind Energy Science Discussions*, pp. 1–18. ISSN: 2366-7621. DOI: 10.5194/wes-2017-37. URL: <https://www.wind-energ-sci-discuss.net/wes-2017-37/>.
- Rathmann, Ole et al. (2017). “Validation of the Revised WAsP Park Model.” In: *WindEurope Conference and Exhibition 2017*. Amsterdam.
- van der Laan, M. P., A. Peña, et al. (2017). “Challenges in simulating coastal effects on an offshore wind farm.” In: *Journal of Physics: Conference Series* 854.1. ISSN: 17426596. DOI: 10.1088/1742-6596/854/1/012046.
- Bossuyt, Ottelien H. G. (2018). “Modelling and validation of wind turbine wake superposition - Using wind farm data.” In:
- Ollier, S. J., S. J. Watson, and C. Montavon (2018). “Atmospheric gravity wave impacts on an offshore wind farm.” In: *Journal of Physics: Conference Series* 1037.7. ISSN: 17426596. DOI: 10.1088/1742-6596/1037/7/072050.
- DTU (2019). *PyWake*. Web. URL: <http://doi.org/10.5281/zenodo.2562662>.
- Energy, DTU Wind (2019). “Automated validation report for PyWake DTU Wind Energy E-report.” In: February.
- Hijmans, Robert J. (2019). *Database of Global Administrative Areas*. Web. URL: <https://gadm.org/index.html>.
- Poulsen, Lina (2019). *Validation of wind farm parametrization in WRF using wind farm data Wind Energy Master Report*.
- Skamarock, William C. et al. (2019). *A Description of the Advanced Research WRF Model Version 4*. Tech. rep. National Center for Atmospheric Research.